Université de Montréal

Reflected Light of Exoplanets - A Case Study of WASP-43b using the Hubble Space Telescope

par

Prashansa Gupta

Département de Physique
Faculté des arts et des sciences

Mémoire présenté en vue de l'obtention du grade de
Maître ès sciences (M.Sc.)
en Physique

December 24, 2019

Université de Montréal

Faculté des études supérieures et postdoctorales

Ce mémoire intitulé

Reflected Light of Exoplanets - A Case Study of WASP-43b using the Hubble Space Telescope

présenté par

Prashansa Gupta

a été évalué par un jury composé des personnes suivantes :

Nicole St-Louis
(président-rapporteur)

Björn Benneke
(directeur de recherche)

David Lafrenière
(membre du jury)

Sommaire

Avec près de 4000 exoplanètes connues, le domaine est passé de simplement détecter des exoplanètes à étudier leurs propriétés atmosphériques. Cependant, les spectres en lumières réfléchies de ces objets sont encore mal compris. Les exoplanètes réfléchissent une partie de la lumière qu'elles reçoivent de leur étoile, selon les propriétés de l'atmosphère, ce qui affecte le budget énergétique de la planète. Les Jupiters chaudes, c'est-à-dire des planètes de types Jupiter avec des périodes orbitales très courtes, sont les cibles les plus faciles à observer par spectroscopie des éclipses. L'albédo est une mesure directe de la lumière réfléchie qui peut être mesurée pendant que la planète passe derrière l'étoile hôte. Dans leur cas spécifique, une incohérence apparente, appelée le problème d'albédo des Jupiters chaudes, reste non résolu. Alors que les géantes gazeuses du système solaire ont des albédos de Bond inférieurs aux albédos géométriques, les mesures dans le visible et l'infrarouges pour HD 189733b et HD 209458b indiquent le contraire. Ceci pourrait être expliqué par des albédos géométriques plus élevés à des longueurs d'onde UV/visibles hors de la bande passante de Kepler, mais très peu de mesures existent pour corroborer cela. Ce mémoire présente le spectre de réflexion complet de WASP-43b, incluant 3 mesures d'éclipse obtenues par le HST (290-570 nm) ainsi que 28 obtenues par la mission TESS (600-1000 nm). Lorsque combinées avec les observations Spitzer ou les observations d'éclipse du JWST à venir, ces mesures répondront à des questions-clés concernant la structure et composition atmosphérique de la planète, le budget énergétique global et sa circulation.
Mots-clés: : planètes et satellites: atmosphères - étoiles: techniques individuelles (WASP-43): techniques photométriques

Summary

With nearly 4000 exoplanets known, the field has evolved from merely detecting exoplanets to actually probing atmospheric properties. However, reflected light spectra from these objects are still not fully understood. Exoplanets reflect a portion of the light that they receive from the star, the amount of which depends on the properties of the atmosphere and in turn affects the energy budget of the planet. Hot Jupiters, i.e. Jupiter-like planets giants with very short orbital periods are the easiest targets amenable to eclipse spectroscopy. Albedo is a direct measure of reflected light that can be measured while the planet eclipses behind the host star. In the specific case of these intriguing planets, an apparent inconsistency, termed as the hot Jupiter Albedo Problem, remains unsolved. While Solar System gas giants show Bond albedos lower than geometric albedos, the measurements from optical and infrared instruments for HD 189733b and HD 209458b show the opposite. This phenomenon has the potential to be explained by higher geometric albedos at UV/optical wavelengths outside the Kepler bandpass, but very few measurements exist to corroborate this. This thesis presents WASP-43b's full reflection spectrum, including 3 eclipse measurements obtained by the HST (290-570 nm) along with 28 obtained by the TESS mission (600-1000 nm). When combined with the Spitzer or the upcoming JWST's eclipse observations, these measurements will answer key questions about the planet's atmospheric composition and structure, global energy budget and circulation.
Keywords: planets and satellites: atmospheres - stars: individual (WASP-43)-techniques: photometric

Contents

List of tables

List of figures

Acknowledgements

I would like to acknowledge my indebtedness and render my warmest thanks to my supervisor Björn Benneke, who made my wish to study exoplanets come true. I got the opportunity to work in the field, learn from one of the most successful exoplanet scientist, and in the end work towards an actual contribution to exoplanet science in terms of the paper that will be published soon. I am grateful to him for always showing support and enthusiasm, steering me in the right direction and keeping his door open for all my questions.

Not only was I a part of an amazing research group, I was a part of IREx, one of Canada's leading research centre for exoplanet research. I am grateful that I was in the company of amazing researchers like René Doyon, Andrew Cumming, Nicolas Cowan, David Lafrenière, Jonathan Gagné, Loic Albert and Étienne Artigau with whom I have had many useful discussions over these years, who have always supported my achievements and encouraged my questions.

This thesis has benefitted from comments by the review committee members, Nicole St-Louis (President) and David Lafrenière. I would like to take this opportunity to thank them.

I have always involved myself in public outreach and astronomy education with an aim to give back to the society, and I am grateful to Marie-Eve Naud, Frédérique Baron and Nathalie Ouellette who have given me multiple opportunities to interact with the public in Montreal. I have enjoyed every bit of the events be it the Eureka festival, the CAN-Yes presentations and numerous others that we organized in the two years, while also learning so much from them.

I am grateful to Sophie Tremblay, who was always so supportive of me, helped me with all the paperwork anytime I asked, and shared amazing conversations and food stories.

This thesis would not have been possible without a constant support system from my 'work-friends', as they are called. The amazing combination of Simon-Gabriel (the)Beauvais, Stefan Pelletier, Jonathan Chan, Merrin Peterson, Steven Rogowski and Caroline Piaulet kept me going through, everyday at work. I am glad to have them in my life. A special mention to Neil Cook for being so amazingly kind and caring right from my first day as a newcomer to Canada, unwavering support and humility.

The person with the greatest indirect contribution to this work is my mother, Madhulika Gupta, who taught me the love of science and especially physics. I express my profound gratitude to her, my father Anupam Gupta and my sister Shailja Gupta, for their unshakeable support and belief in me, even though they lived half the world away from me. This accomplishment would not have been possible without them.

This thesis has been written in the Department of Physics at University of Montreal, to which I am thankful for providing an amazing campus, facilities and making my degree a success.

Chapter 1

Introduction

The idea of innumerable worlds, apart from our own, existing in the cosmos is venerably old, dating back to the Greek civilization. After remaining in the realm of pure speculation, it entered the territory of real scientific explorations in the second half of the twentieth century and led to the confirmed discovery of the first exoplanet in the early 1990s. A new field of exoplanet research was brought to light that boosted interest in not only our own Solar System and its origins but also in search for life in the Universe.

Shining by reflected starlight, exoplanets are a million or more times fainter than their host stars and are at angular separations from their accompanying star of, at most, a few seconds of arc, depending on their distance. This combination makes direct detection extraordinarily difficult, especially at optical wavelengths where the star to planet intensity ratio is large, more so from the ground, given the perturbing effect of the Earth's atmosphere.

Alternatively, astronomers shifted focus towards indirect detection methods. The one based on dynamical perturbation of the star by its orbiting planet delivered the first tangible results. Radio pulsar timing achieved the first convincing detection of planetary mass bodies beyond the Solar System (Wolszczan & Frail, 1992). High accuracy radial velocity (Doppler) measurements yielded the first suggestions of planetary mass objects surrounding main sequence stars from the late 1980s (Campbell et al., 1988; Latham et al., 1989; Hatzes & Cochran, 1993) with the first unambiguous detection in 1995 (Mayor & Queloz, 1995).

This discovery precipitated a changing mindset and the upcoming two decades saw a wealth of planets show up. In the photometric search for transiting exoplanets, the first transit of a previously detected exoplanet was reported in 1999 (Charbonneau et al., 1999), the first discovery by transit photometry in 2003 (Konacki et al., 2003), the first of the wide field bright star survey discoveries in 2004 (Alonso et al., 2004), and the first discovery from space observations in 2008 (Barge et al., 2008). Advances in Doppler measurements,

photometry, microlensing, timing, imaging and astrometry have since been instrumental in discovering planets in large numbers.

As of November 1, 2019, more than 4100 confirmed exoplanets are catalogued with 671 multiple exoplanetary systems. Figure 1.1 shows all the existing exoplanet detection methods along with estimates of the number of exoplanets discovered by each and the sensitivity in terms of mass. We can see that the transit method has been the most successful closely followed by the radial velocity method. We are constantly pushing towards Earth mass sensitivity with the upcoming technologies.

Since the existence of exoplanets was firmly established, the adventure of exploring the exoplanet's physical characteristics had to begin in earnest. Thus, over the years, the theme of exoplanets has shifted from mere detection to an in-depth characterization. An exoplanet's physical properties such as density, atmospheric composition, temperature can be measured for a subset of planets - hot planets, especially transiting hot planets.

Based on present numbers from radial velocity surveys, at least 5-10% of Solar-type stars in the Solar neighbourhood harbour massive planets. A much higher fraction, about 30% or more, may have planets of lower mass or with larger orbital radii. If these numbers can be extrapolated, the planets in our Galaxy alone reach many billions!

With such a huge sample size at hand, studies showed that exoplanets do not adhere to the individual or system properties that can be easily extrapolated from those of the Solar System. We have found an astonishing range of observed masses, semi-major axes and orbital eccentricities. Half of the planets for which we have estimated masses, for example, have masses of Jupiter (0.3-3 M_j). Most of these planets orbit closer than Mercury orbits the Sun (0.39 au). Others are located far out at distances of 100 au or more. Orbits highly inclined to the star's equatorial plane occur reasonably frequently, some even in retrograde orbits. Exoplanets are being found around a variety of host stellar types be it low mass stars, low metallicity stars or white dwarfs. Their internal structures vary a lot - gas giants with their outer envelopes stripped off, water worlds and carbon dominated planets, may all exist.

A wide variety in the kind of exoplanets found points to a huge diversity of exoplanet atmospheres. Even though the atmosphere constitutes only a tiny fraction of the planet's mass, it has an immense importance in determining the physical properties of planets, evolution with time and physical appearance. Atmospheres greatly influence planet energy balance, for example, the relative importance of gaseous absorption or scattering from clouds or gases dictates a planet's reflectivity (albedo). They impact cooling, as interior

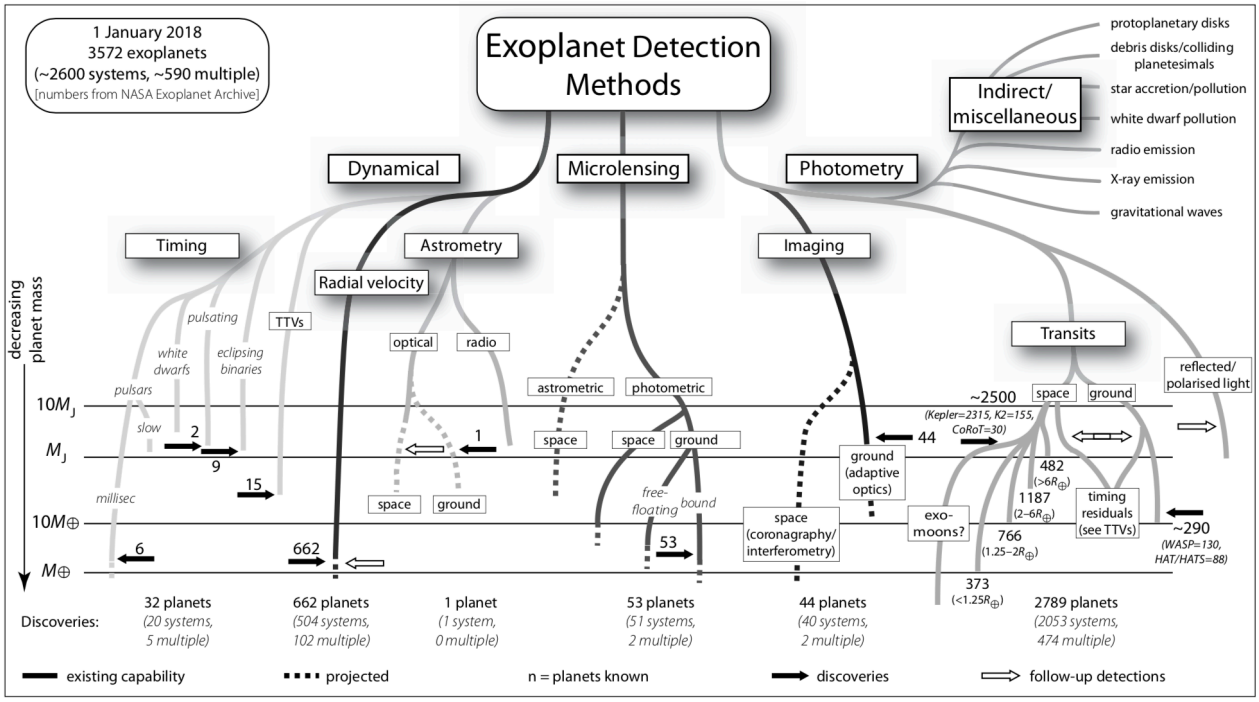

Fig. 1.1. Exoplanet detection methods. The lower limits of the lines indicate masses within reach of present measurements (solid lines), and those that might be expected within the next few years (dashed). The logarithmic mass scale is shown on the left. Miscellaneous signatures to the upper right are less well quantified in mass terms. Solid arrows show relevant discoveries. Open arrows indicate measurements of previously-detected systems. Numbers are from the NASA Exoplanet Archive, 2018 January 1. Figure adopted from The Exoplanet Handbook by Michael Perryman 2018

convection or conduction must give way to radiative atmosphere to lose energy out to space. Their composition tells us the story of the gain and/or loss of volatiles, whether the atmospheres were accreted from the nebula, outgassed later from the interior, lost to space by escape processes and/or regained by the interior.

We can find two broad reasons for studying planetary atmospheres. First, the atmospheres are inherently interesting as they present a variety of physical and chemical processes at work. Various questions come to the forefront: what determines day-night temperature contrast on the planet, why are some atmospheres dominated by clouds and

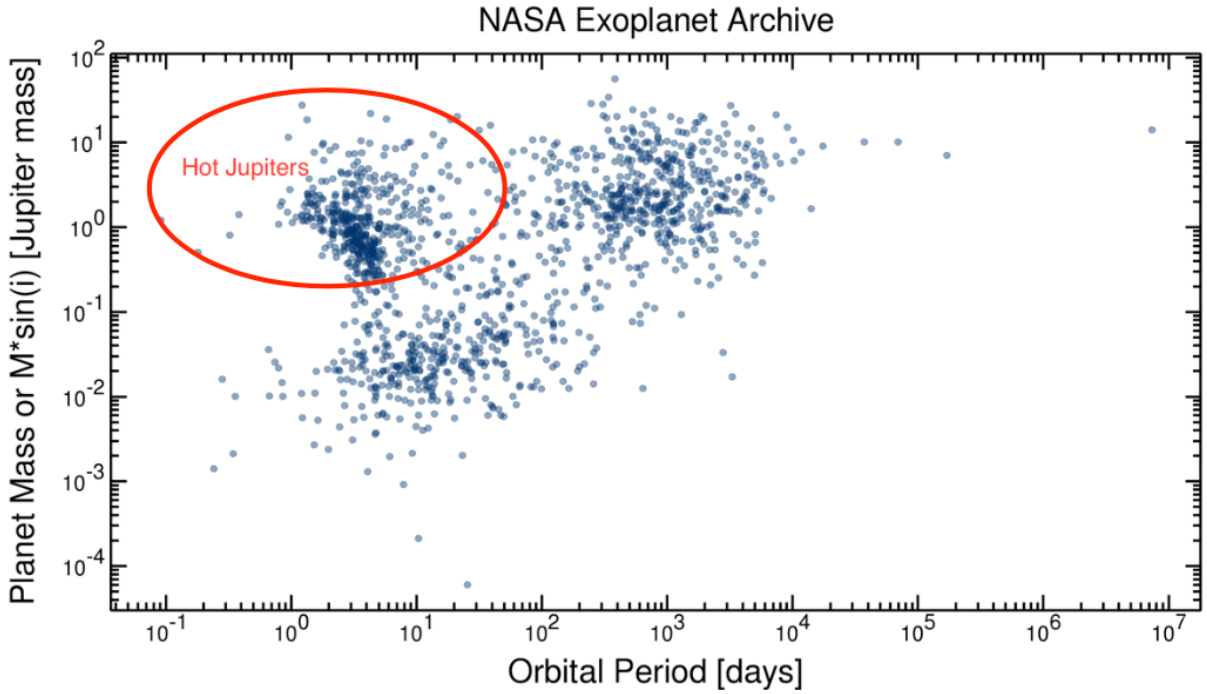

Fig. 1.2. Mass-Orbital Period diagram for confirmed planets as of November 1, 2019. The location of Hot Jupiters is marked. Only objects with mass determinations provided in the NASA exoplanet archive are indicated. Thus many of the confirmed planets are missing, especially in the lower left region of the diagram where, for most of the transiting planets, only radii are available. Objects from all discovery methods are included. Darker points delineate overlapping symbols.

others cloud-free, how fast can winds blow, what sets the temperature structure of the atmosphere, why do some have thermal inversions, how are the chemical abundances of atoms and molecules set, if planets lose their atmosphere can they gain another, and the list continues. The other reason is that atmospheres can tell us about the formation and evolution history of the planet, and by extension our own Earth. For example, the metal enrichment of a giant planet in comparison to its star helps us understand planet formation, noble gases tell us about accretion of primordial volatiles and comparative planetology informs us about divergent evolution tracks.

For the specific purposes of this thesis, we will mostly be concerned with a subset of exoplanets, namely the hot Jupiters. These are the ones readily accessible for atmospheric observations and modelling. Hot Jupiters or short period gas giants, are loosely defined as Jupiter-mass planets with semi-major axis $\leq$ 0.1 au or orbital periods of 1 to 9 days (Gaudi et al., 2005). Because of their close-in orbits, they are significantly heated by stellar irradiation. This proximity enforces strong tidal friction and thus, planets in orbits $\leq$ 10 days are likely tidally locked (Guillot et al., 1996; Parmentier et al., 2015), which means

that their rotation rates are synchronised with their orbital periods. Thus, close-in hot Jupiters show the same face to their star at all times, similar to the Moon in the case of the Earth. Their location in the mass-period diagram for confirmed exoplanets with determined masses is shown in Figure 1.2.

Tidally locked hot Jupiters then have a large day to night irradiation gradient, that consequently allows them to develop a strong atmospheric circulation that advects energy from the dayside to the nightside and reduces this contrast compared to the local radiative equilibrium case. But energy losses due to radiation or damping by winds can prevent a fully efficient redistribution of energy.

The balance between energy transport and energy losses can be understood in terms of timescales (Showman & Guillot, 2002; Komacek & Showman, 2016). The radiative timescale characterises the time it takes for a parcel of gas to lose its energy by radiation, while the wave timescale is the time it takes for gravity waves to travel horizontally over one planetary radius and the drag timescale is the time it takes for the waves or the winds to lose a significant part of their kinetic energy.

Depending on the balance among these scales, two regimes exist 1. If the radiative or drag timescale is smaller than the wave timescale, the atmospheric circulation is characterized by a day to night flow and the temperature map is symmetric around the substellar point and a larger hemispheric temperature contrast exists (Showman & Polvani, 2011; Tsai et al., 2014). 2. Conversely, when radiative and drag times are greater than the wave timescale, the presence of an eastward equatorial jet is expected. The hottest point of the atmosphere lies eastward of the substellar point (the center of the planetary disk as seen from the star), with the entire temperature map shifted eastward in comparison to the local radiative equilibrium case (Showman & Guillot, 2002).

Being irradiated on the same hemisphere from continuous illumination by the host star is a property that also contributes to a rich spatial structure in the climate and the atmospheric composition of these planets. This asymmetry is expected to produce inhomogeneities in the temperature, the chemistry and the cloud coverage (Showman et al., 2009; Kataria et al., 2016; Parmentier et al., 2016) thus providing an opportunity to learn about atmospheric dynamics in a very different regime from that of the Solar System. But, utilizing this opportunity is an extremely challenging task on a technical level. It is typically not possible to spatially resolve the planet from its host star and the star outshines the planet by a factor of at least a thousand to one.

In order to circumvent these issues, astronomers have come up with many creative strategies and made use of the star as a constant reference point. These include transit, eclipse and phase curve methods where, with meticulous observations, the planet's light can be measured relative to a constant baseline flux from the star. The resulting inferences of planetary atmospheric properties are remarkably detailed, given the fact that they are solely based on point sources of light hundreds of parsecs distant.

1.1. Transit Method

The most widely employed technique is the transit method. During a transit, as illustrated in Figure 1.3, the planet passes in front of its host star and blocks a fraction of the star's light equal to the sky projected area of the planet relative to the area of the star, this fractional drop is called the transit depth. Transit measurements are relative in the sense that the flux of the system (star + planet) during transit is compared to the out-of-transit flux. Figure 1.4 shows an example of transit light-curves for the exoplanet HD 209458b.

Under the assumption that exoplanetary orbital planes are aligned at random relative to our line-of-sight, the transit probability for a close-in planet in a circular orbit is R_s/a (Winn, 2010) where R_s is the stellar radius and a is the radius of the orbit. Thus, planets are more likely to transit their host stars when they have short orbital periods (from Kepler's Third Law).

Transit spectra records the flux drop at various wavelengths (Seager & Sasselov, 2000). This wavelength dependence of the transit depth comes about because the atmosphere is opaque at certain wavelengths due to absorption by atoms or molecules . To measure these variations, the light-curve is binned in wavelength into spectrophotometric channels, and the light-curve from each channel is fit separately with a transit model. These measured transit depths a function of wavelength constitute the transmission spectrum. Figure 1.4 illustrates how transit light-curves are measured and modeled at different wavelengths for the case of HD 209458b, followed by Figure 1.5 which shows measurements of transit depth plotted as a function of wavelength, called the spectrum. The transmission spectrum in Figure 1.5 shows the near-infrared transmission spectrum of the hot Jupiter WASP-43b, which has a strong water absorption feature centered at $1.4\mu m$. Thus, through transmission spectroscopy, one can infer the atmospheric composition by studying the absorption features observed.

Carrying out spectroscopy at transit, in general, is more favorable at optical wavelengths where the star is brightest. Spectroscopy at transit relies on the star being the illuminating

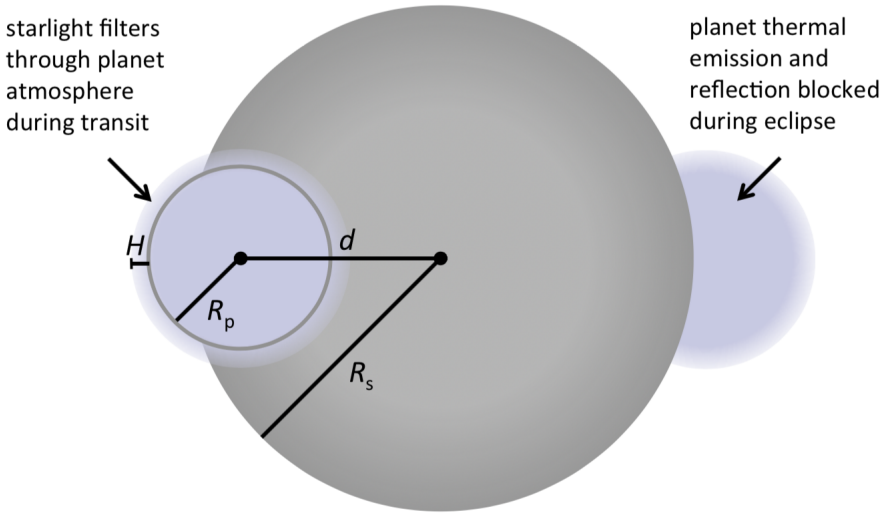

Fig. 1.3. Illustration of a transit and an eclipse geometry. Over the course of the planet's orbit, it periodically passes in front of the star (a transit event) and behind (a secondary eclipse). A few key distances are labeled: the planet and stellar radii, Rp and Rs, the atmospheric scale height H, and the separation of centers in the plane of the sky, d. Figure adopted from Robinson (2017)

source and, all else kept equal, the signal to noise ratio for transit spectroscopy increases as the square root of the brightness of the star. Transit spectroscopy at long infrared wavelengths is much more difficult since the illuminating star is much fainter. An exception here will be M dwarfs which are brightest in the near infrared (~ 2 μm).

Theoretical models for transmission spectra require radiative transfer calculations for light on the slant path through the planet's atmosphere (Seager & Sasselov, 2000), which is a computationally intensive task to do. We can also make a rough prediction of the size of features in the transmission spectrum based on the atmospheric scale height H. The scale height is the change in altitude over which the pressure drops by a factor of e. If we assume hydrostatic equilibrium, and use the ideal gas law,

$$H = \frac{K_B T_{eq}}{\mu g}$$

where K_B is the Boltzmann constant, T_{eq} is the planet's equilibrium temperature, μ is the mean molecular mass and g is the surface gravity.

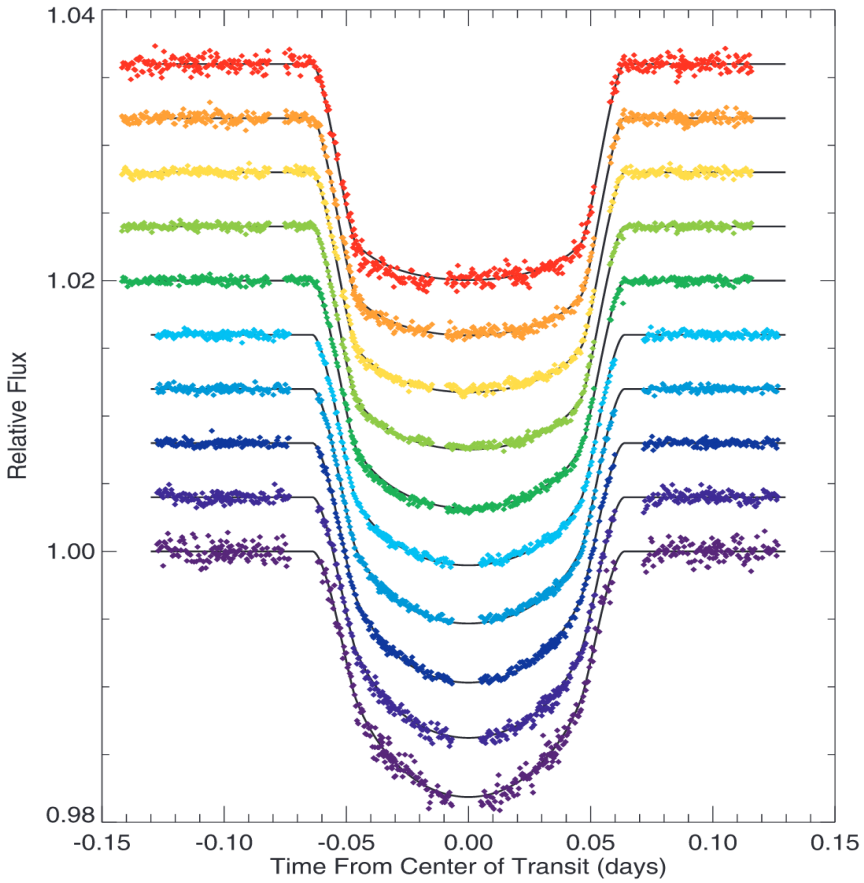

Fig. 1.4. Transit light-curves of HD 209458b obtained using the STIS instrument onboard the Hubble Space Telescope. The figure shows normalized data for 10 bandpasses in the range 290 to 1020 nm. Also overplotted are the theoretical transit curves using the best-fit parameters from a simultaneous fit of all bandpasses. Each successive transit curve is offset by 0.004. The color coding is according to the colors of the visual spectrum, with red representing 1020nm and the violet representing 290 nm. Figure adopted from Knutson et al. (2007a)

The amplitude of spectral features in transmission is then,

$$\delta_\lambda = \frac{(R_p + nH)^2}{R_s^2} - \frac{R_p^2}{R_s^2}$$
$$\approx \frac{2nR_pH}{R_s^2}$$

where n is the number of scale heights crossed at wavelengths with high opacity. We ignore the $(nH)^2$ term since it is small in comparison to the radius of the star R_s.

This rough estimate then shows that the ideal candidates for transmission spectroscopy will have high equilibrium temperatures, small host stars, low surface gravity and low mean

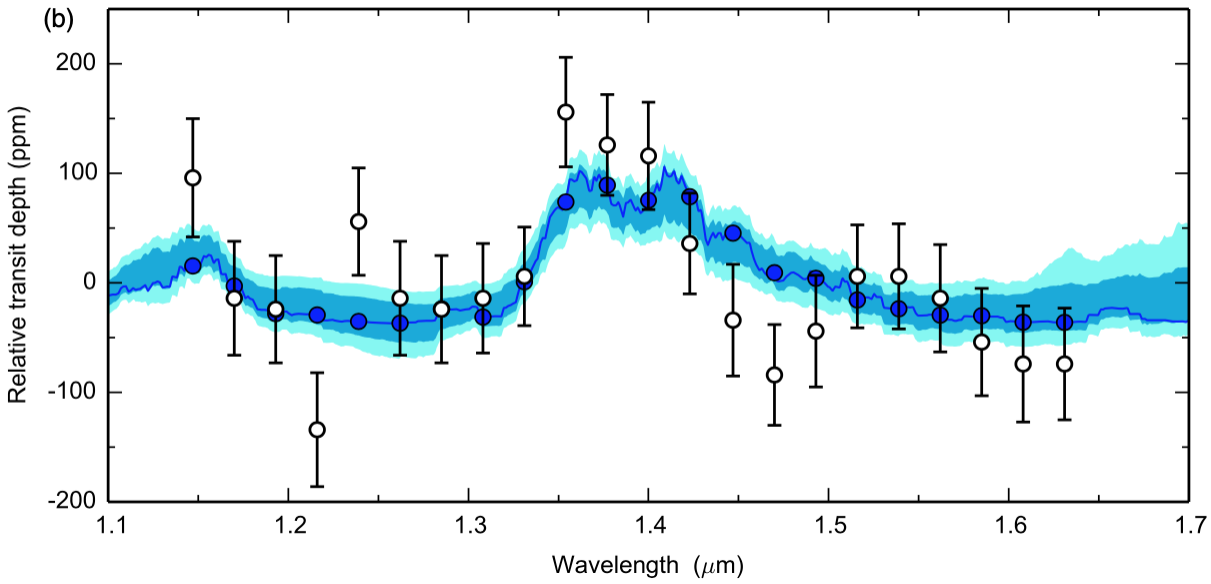

Fig. 1.5. Transmission spectrum for the hot Jupiter WASP-43b using data obtained by the WFC3 instrument ($1.1 - 1.7\mu m$) onboard the Hubble Space Telescope. The blue line corresponds to the best fit model, and dark and light blue shading correspond to the $1-$ and $2-\sigma$ confidence intervals from an atmospheric retrieval. The retrieval analysis explores the parameter space of temperature profiles and chemical compositions that match the data. In this case, water absorption-the broad feature at $1.4\mu m$ is detected at high confidence ($> 5\sigma$).The retrieval constrains the water abundance to be between 0.4 and 3.5× Solar at 1σ confidence.

molecular mass composition (mostly hydrogen dominated). In these ideal cases, the depth is about 0.1%.

1.2. Eclipse Method

In order to detect and characterize exoplanets, we need to first distinguish their light from that of the much more intense nearby source, the host star. If the orbital configuration is favorable, we can infer the relative contribution of the light from the exoplanet during secondary eclipse or occultations (Figure 1.3). As the planet is eclipsed behind the host star, a wavelength dependent flux drop is observed. This drop is obtained by subtracting flux of the system before or after secondary eclipse from that during secondary eclipse.

Short period, close-in hot Jupiters will have a higher probability to produce eclipses and the duration of a few hours allows inexpensive and time efficient measurements. They are close enough to the host star to receive large amounts of incident flux and thus, with temperatures ranging from 1000-2000 K, reflect and emit within detectable limits. Since, they are tidally locked, we monitor the same side at each eclipse event which adds

repeatability of results if the atmosphere is in equilibrium.

There are three main quantities that we can measure during a secondary eclipse - the time when it occurs, its depth and its wavelength dependence.

For timing, we need the eccentricity and the orientation of the orbit, which are measured using radial velocity observations or we can make a reasonable assumption of a circular orbit and look for a eclipse half a period after the transit occurs. Conversely, the measurement of the time and duration carries information on the eccentricity of the orbit.

Considering that the eccentricity, the argument of periastron and the time of central eclipse are accurate enough, and the systematic noises were kept down to reasonable values, any departures from measured times can then be ascribed to the non-uniform illuminaton of the day side of the planet (Williams et al., 2006; Agol et al., 2010; Dobbs-Dixon et al., 2015). One possibility for this non-uniformity is an eastward jet (east defined with the direction of planetary rotation) that has long been predicted from several atmospheric models (Showman & Guillot, 2002; Cooper & Showman, 2006; Cho et al., 2003; Burkert et al., 2005). This non-uniformity of the dayside changes both the ingress and egress profiles, which when fitted to a symmetrical eclipse model show measurable offsets of the time of central eclipse. If the precision is good enough and the ingress and egress profiles sufficiently sampled, it is possible to expand this technique and map the visible hemisphere of the planet. Figure 1.6 shows an example of models of departure from measured eclipse times due to non-uniform illumination of the dayside for the case of HD 209458b. Both the ingress and egress profiles show a flux difference of about 3 to 6 %.

The eclipse depth gives the relative contribution of the flux coming from the planet F_p/F_s, the ratio of the flux of the planet to that of the star. When reflected light is dominant, the eclipse depth is given by

$$\frac{F_p}{F_s} = A_g(\lambda) \left(\frac{R_p}{a}\right)^2 \phi(\theta)$$

where $A_g(\lambda)$ is the geometric albedo, R_p is the planetary radius, a is the semi major axis and $\phi(\theta)$ is the phase function. The geometric albedo $A_g(\lambda)$ is the ratio of brightness at zero phase (i.e., seen from the star) to that of a fully reflecting, diffusively scattering (Lambertian) flat disk with the same cross section. For a Lambert sphere, $A_g(\lambda) = 2/3$. The relevant phase function is given by (Charbonneau et al., 1999),

$$\phi(\theta) = (\sin\theta + (\pi - \theta)\cos\theta)/\pi,$$

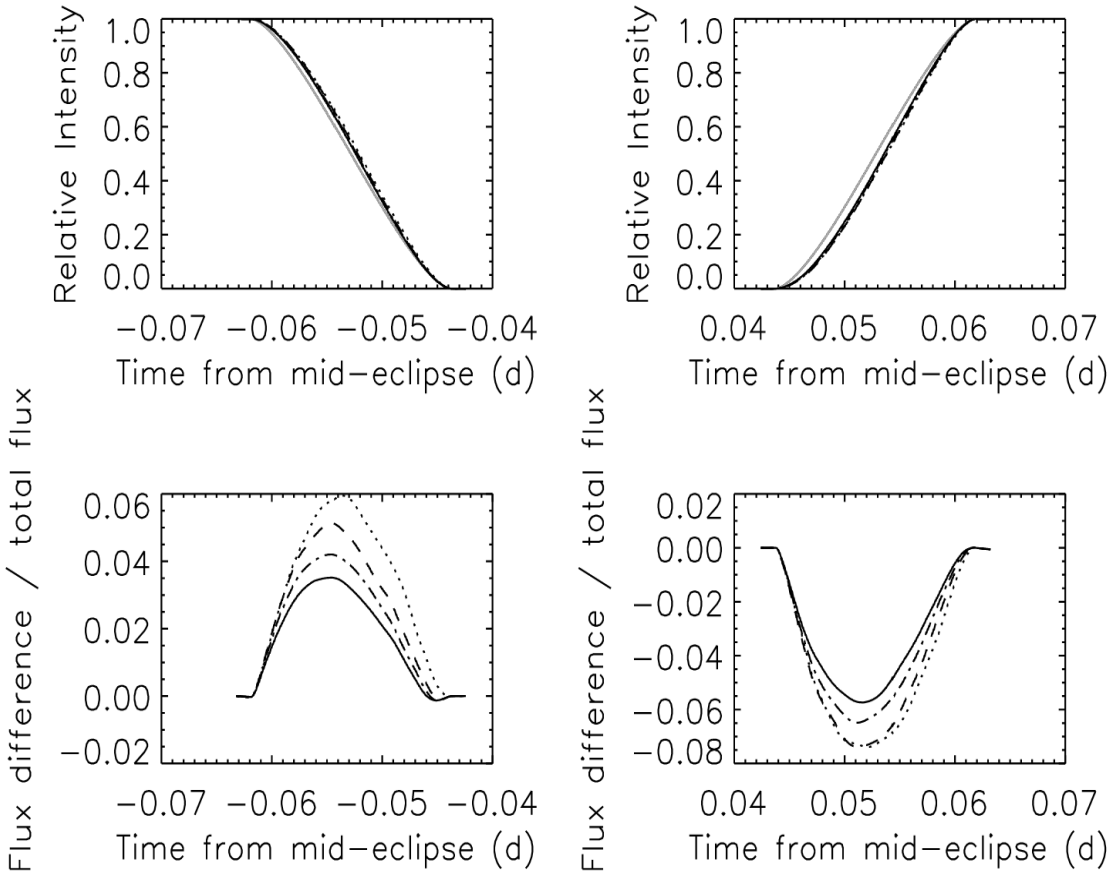

Fig. 1.6. Models of departure from measured eclipse times due to non-uniform illumination of the day side of HD 209458b. *Upper Left*: Ingress portion of the secondary eclipse light-curves, assuming a uniform flux distribution (solid gray line) and model for the spatial flux variation (dashed lines overlying each other). *Lower Left*: The relative differences in the curves resulting from the the non-uniform model to the prediction of the uniform flux distribution, for the four Spitzer/IRAC band passes ($3.6\mu m$, dotted lines; $4.5\mu m$, dashed lines; $5.8\mu m$, dash-dotted lines; and $8.0\mu m$, solid lines). The right panels depict these curves and their differences at egress. Figure adopted from Williams et al. (2006)

with

$$cos\theta = -\sin i \sin(2\pi\beta)$$

where $\theta \in [0,\pi]$ is the angle between star and observer subtended at the planet, $i \in [0,\pi/2]$ is the orbit inclination and $\beta \in [0,1]$ is the orbital phase, with $\beta = 0$ at the time of radial velocity maximum.

If the thermal emission dominates (either reprocessed stellar irradiation or internal heat), the observed eclipse depth is

$$\frac{F_p}{F_s} = \frac{B(\lambda, T_{d,p})}{B(\lambda, T_s)} \left(\frac{R_p}{R_s}\right)^2$$

where $B(\lambda, T_s)$ and $B(\lambda, T_{d,p})$ are blackbody emissions of the star and planetary dayside at brightness temperatures of T_s and $T_{d,p}$ respectively. Since the planet is cooler than the star, the flux ratio will be larger at longer wavelengths. In general, the eclipse depth is a combination of thermal emission and reflected light i.e. a combination of the above equations.

Also, this equation is only a first-order approximation of the planet signal. More complex features come into play due to the atmosphere's changing opacity with wavelength. The emitted light that is recorded comes from the photosphere of the planet where the optical depth is of order unity. But at another opaque wavelength, the photosphere might be at a different altitude where the temperature might differ from the equilibrium temperature. Thus, the spectra will show a change in the flux received.

The size and shape of spectral features depends on the exact temperature-pressure profile of the atmosphere. For example, if the temperature increases with altitude it is called a thermal inversion or a stratosphere. Here, the spectral features seen are emission features rather than absorption. Thus, thermal emission spectroscopy is a powerful probe of temperature structure in addition to atmospheric composition.

In case the planet re-emission is non-isothermal then different dayside locations will emit at different blackbody temperatures and the resulting emission will not be a Planck curve. We then need to take into account the sum of blackbodies with different temperatures at concentric annuli, otherwise we might underestimate the thermal emission in the optical (Schwartz & Cowan, 2015). Estimation of the dayside temperature is necessary to extrapolate the thermal flux (typically measured in the near IR) to optical wavelengths in order to isolate the contribution from the reflected light with the goal of measuring the geometric albedo.

Following Cowan & Agol (2011a), we define the equilibrium temperature of the sub-stellar point of the planet as

$$T_o = T_s \sqrt{(R_s/a)}$$

which can then be used to estimate the temperature of the planet, given the Bond Albedo (A_b: fraction of all the incident flux from the star at all wavelengths that is absorbed by the planet) and a parameterization of the efficiency of the transport of incident flux from the sub-stellar point to the nightside.

The case of zero albedo and 100% efficiency is used to define the equilibrium case and we obtain $T_{eq} = T_o/\sqrt{2}$. With known stellar parameters, one can then estimate the dayside

temperature and compare this value to the observed value which can then serve, in principle as an estimate of the efficiency factor. Solving the energy budget, however, has been a challenging task (Schwartz & Cowan, 2015; Schwartz et al., 2017).

The wavelength dependence of the eclipse depth can also be exploited. Extending observations to different wavelengths can help distinguish the fraction of light received from reflection and thermal emission. At near-infrared wavelengths most, if not all, light is thermal emission and in the bluest visible colors the light is reflected. Ideally, observations at all wavelengths will be needed to estimate the Bond albedo and also to study the geometric albedo at different colors. Combining data from different wavelength bins, the dayside emission spectra builds up. This will have features imprinted that will reveal the components of the atmosphere.

The detection of secondary eclipse of an exoplanet is a very challenging task since even for the most favorable cases of hot Jupiters observed in the near infrared, the depths are typically only a few tens of a percent. In the optical (regardless of origin - thermal or reflected) the measured depths are below 100 ppm.

1.3. Phase Curves

For the case of tidally locked exoplanets, a phase curve measures the change in the planetary system's flux with planetary phase as seen from Earth over an entire orbital period, which mathematically, is the longitudinal distribution of flux from the exoplanetary atmosphere convolved with the geometric projection to the observer (Cowan & Agol, 2008). This brightness distribution is a combination of emitted and reflected light in the particular bandpass of observation. Over the course of an orbit, we observe different hemispheres of the planet, ranging from its dayside (before and after it eclipses behind the star) to its nightside (when it transits in front of the star). The nightside is usually colder and therefore dimmer than the dayside. The thermal emission of the planet can be used to probe temperature inhomogeneities. The wavelength dependence and shape of the phase curve help determine the inhomogeneous chemical composition and cloud coverage.

At optical wavelengths, the brightness is dominated by reflected light, thus the optical phase curve informs us about the longitudinal variation of the planet's albedo (reflectivity) and constrains the relative abundances of condensates or aerosols. At infrared wavelengths, the brightness is dominated by thermal emission, which means that the phase curve has information about the longitudinal variation of the planet's temperature and chemical composition. The molecular features shape the spectral variation of the thermal phase curves. Inside a molecular absorption band, a phase curve probes low pressures (high

altitudes) while probing deeper outside a molecular absorption band (Showman et al., 2009; Kataria et al., 2015). Thus, multiwavelength phase curves probe the 2D - longitude and altitude - thermal and chemical structure of the atmosphere (Knutson et al., 2009; Stevenson et al., 2014b, 2017)

Using phase curve observations, three parameters can usually be retrieved (Cowan & Agol, 2008; Demory et al., 2013; Knutson et al., 2009, 2012). For transiting planets, they are the secondary eclipse depth, the phase curve offset (phase of the maximum of the phase curve as compared to secondary eclipse) and the phase curve relative amplitude, $A_F = (F_{p,Max} - F_{p,Min})/F_{p,Max}$. The secondary eclipse depth yields the brightness of the dayside hemisphere and is a reference to calculate A_F. Offsets of flux minima and maxima in light-curves provide information about the longitudinal displacement of hottest and coldest regions from the substellar and anti-stellar point.

Exoplanets whose dynamics lead to an equalized temperature at all longitudes will exhibit flat light-curves whereas those with order unity day/night temperature differences will present high amplitude phase variations throughout the orbit, comparable to the depth of the secondary eclipse. Tidally locked, short period exoplanets have a short radiative timescale, a weak Coriolis force, and an input of energy at large scale that makes them likely to have planetary scale atmospheric features that can be observed in the hemispherically averaged planetary flux (Showman & Guillot, 2002).

The composition of the atmosphere plays an important role in shaping the phase curve of exoplanets. If the abundance of metals in the atmosphere is increased, the metallicity increases the opacities : 1. the atmospheric layers probed are shifted to smaller pressures where the radiative timescale is smaller leading to a large phase curve amplitude and a smaller phase curve offset 2. the enhanced opacities make the atmosphere warmer and lead to a smaller radiative timescale. For WASP-43b, Global Circulation Models with a metallicity of five times Solar provide a better, but not satisfactory, match to observations compared to models assuming a Solar metallicity (Kataria et al., 2015)

For the case of small planets, the atmospheric composition can be very diverse and the mean molecular weight of the atmosphere is expected to impact both the radiative and wave timescale. Zhang & Showman (2017) show that when the mean molecular weight is increased, the day/night temperature contrast is expected to increase and the eastward shift of the hot spot is expected to decrease. In real planets, atmospheres with different mean molecular weight will have a very different composition leading to several orders of magnitude worth of variations in opacities and potentiallly a comparable or stronger effect

than the effect of the mean molecular weight alone.

When in chemical equilibrium, temperature inhomogeneities are associated with chemical composition inhomogeneities. Given an atomic composition, the equilibrium can favor a variety of molecules at different pressures and temperatures, thus, a day/night temperature contrast on a tidally locked planet could result in a corresponding day/night chemical gradient. Such a large-scale change in chemistry is expected to trigger a change in the opacities and consequently affect the offset and amplitude of the phase curve. Horizontal and vertical advection are expected to further complicate this scenario.

As inferred from observations, the large temperature variations in the atmosphere of tidally locked planets in close-in orbits are responsible for large longitudinal inhomogeneities in their cloud coverage (Demory et al., 2013; Shporer & Hu, 2015). Some species that condense in the cold nightside must be in gaseous form in the hot dayside (Parmentier et al., 2013). Now, since the temperature map of hot Jupiters is not symmetric but shifted eastward, the western part is usually cold and clouds can form there. The optical phase curve will then be dominated by a bright reflective part of the dayside atmosphere where clouds are present, leading to a phase curve peaking after the secondary eclipse, opposite to the thermal phase curve (Hu et al., 2015; Garcia Munoz & Isaak, 2015; Webber et al., 2015). The longitudinal distribution for a given type of cloud in the dayside is determined to first order by the thermal structure of the planet and the cloud-specific condensation temperature (Lee et al., 2016). If the thermal structure is known, either by observing a thermal phase curve or by modeling the temperature distribution a priori, the cloud map derived from the reflected light-curve can be used to constrain the cloud chemical composition (Oreshenko et al., 2016; Parmentier et al., 2016).

Clouds, along with being reflective, are also expected to affect the thermal emission of the planet. If clouds are present on the nightside, they produce a large opacity gradient between the day and night that can suppress the thermal emission from cloudy regions by raising the photosphere to low pressures. Consequently, clouds are then expected to increase the phase curve amplitude and decrease the phase curve offset of hot Jupiters, even if only present on the nightside. In the presence of clouds, the brightest hemisphere is not necessarily the hottest one, and the shift of the maximum of thermal phase curves does not track the shift of the hottest point of the planet anymore. Any inference of the thermal structure and the atmospheric composition based on a phase offset and a day/night contrast gleaned from only a thermal phase curve can be highly biased by the presence of clouds, therefore, the optical phase curve that probes the planetary albedo as a function of longitude is absolutely necessary. Atmospheric properties can also be time variable, implying that the phase curve

is time-dependent also. Atmospheric variability has not been widely characterized, given the overheads associated with observing full orbit phase curves and the time needed to constrain differences between phase curves.

1.4. Major Results and Observational Achievements

In this section, we discuss the major observational highlights for transmission, emission and phase curve spectroscopy in categories of atmospheric composition, abundances, climate and condensates such as clouds and/or hazes.

1.4.1. Atmospheric Composition

Expectations

The Solar System informs us that the atmospheric composition can vary widely. Even so, we can still try to make educated guesses about the possible compositions based on the building blocks of planet formation that come from disks of gas and dust surrounding young stars. The protoplanetary disk is expected to have a similar composition as the host star, predominantly hydrogen and helium with some amounts of metals like oxygen, carbon and nitrogen (Anders & Grevesse, 1989).

These main constituents are then expected to combine into H_2, H_2O, CO, CO_2, CH_4, NH_3, O_2, and N_2 depending on the temperature, pressure and composition of the planet's atmosphere (Moses et al., 2013). Most of these species have strong absorption features and are thus easily detectable, as illustrated in Figure 1.7. In this figure, the predicted opacity of dominant absorbers for a Solar composition atmosphere at 1500 K (a typical hot Jupiter) is shown. There are several species that are less abundant but still detectable because of their large absorption cross section like the alkali metals (Na and K, at optical wavelengths) and TiO and VO. H_2O and CO are dominant at near-infrared wavelengths. At lower atmospheric temperatures, CH_4 and NH_3 become more abundant.

Observations

Transmission and emission spectroscopy have revealed the compositions of exoplanet atmospheres, beginning with the first atmospheric detection in HD 209458b (Charbonneau et al., 2002) and the secondary eclipses of TrES-1b and HD 209458b (Charbonneau et al., 2005; Deming et al., 2005). After these initial discoveries, many ground-based and space-based observations of transiting exoplanets revealed Na (Huitson et al., 2012), K

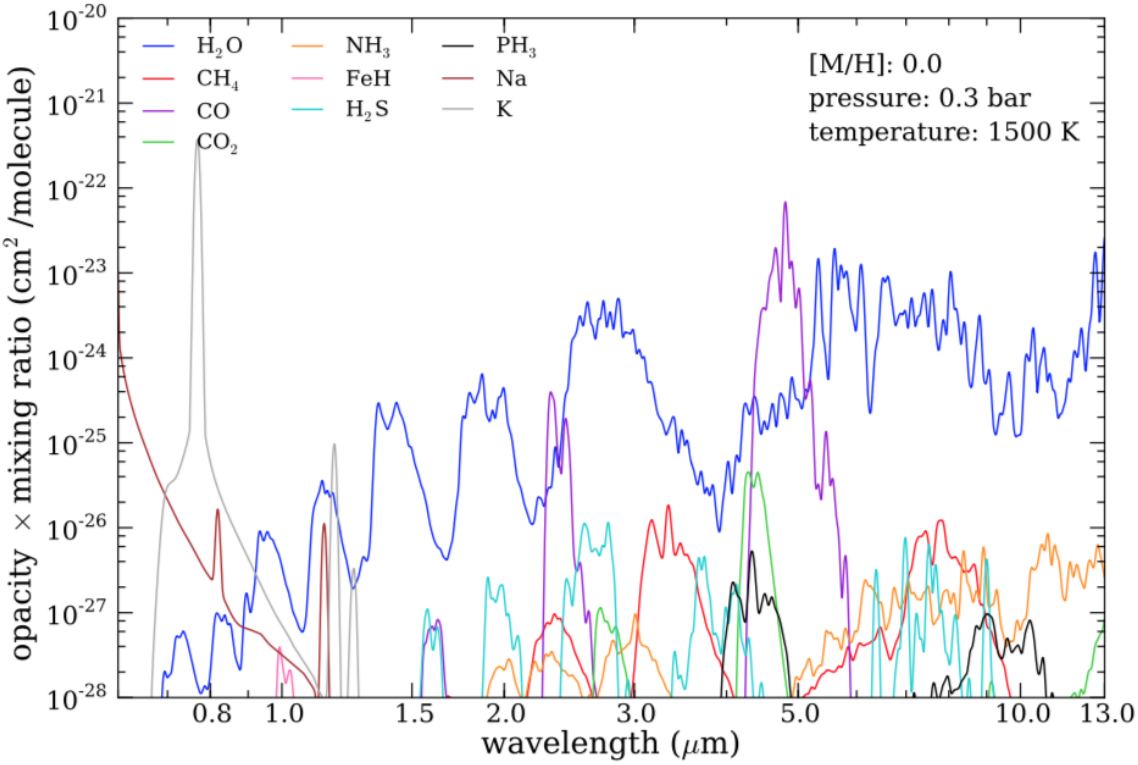

Fig. 1.7. Opacities for a Solar composition atmosphere in chemical equilibrium at 1500K and 0.3 bar. Even though H and He dominate the atmospheric composition, they only have collision induced continuum opacity at infra red wavelengths, and the spectrum is instead dominated by the molecular and atomic species shown here. (Kreidberg, 2018)

(Sing et al., 2011a), H_2O (Deming et al., 2013), CO_2 (Snellen et al., 2008) and recent weak evidence for TiO (e.g. Evans et al. 2016; Nugroho et al. 2017; Sedaghati et al. 2017) in hot Jupiter atmospheres.

The Hubble Space Telescope (HST) has enabled high precision spectroscopy with the Wide Field Camera 3 (WFC3) grism mode from 1.1 μm to 1.7 μm (e.g. Berta et al. 2012). This bandpass encompasses a broad H_2O feature, a molecule that is most commonly observed and that is visible both in transmission and secondary eclipse spectra of exoplanets (e.g. Deming et al. 2013; Kreidberg et al. 2014a; Huitson et al. 2013; Birkby et al. 2013; Line et al. 2016; Evans et al. 2016). WFC3 observations have provided the most successful detections of molecular features because of the combination of the instrument's state-of-the-art measurement precision and water's strong absorption features. Atmospheric abundance retrievals have been applied to these WFC3 measurements to provide the H_2O abundance in planet atmospheres, a proxy for atmospheric metallicity if one assumes the

elements heavier than Helium have constant number fractions relative to each other at near-Solar values. These studies then have been used to constrain the planet-mass versus metallicity relation (e.g. Kreidberg et al. 2014a; Line et al. 2016; Wakeford et al. 2017b) as well as to study the factors that contribute to the thickness of clouds in hot Jupiter atmospheres (Sing et al., 2016).

Hydrogen has also been detected. Observation of Lyman-α with HST's STIS instrument revealed large exospheres of escaping atomic hydrogen around hot planets (Vidal-Madjar et al., 2003; Ehrenreich et al., 2015), which also contained ionized metals (e.g. OI, CII Vidal-Madjar et al. 2004). The presence of molecular hydrogen was inferred from a Rayleigh scattering signature in the spectrum of HD 209458b (Lecavelier Des Etangs et al., 2008b). However, since condensates can also cause Rayleigh scattering, it is not certain that H_2 is the culprit.

Carbon bearing molecules are more difficult to detect mainly due to the wavelength range accessible by current observing facilities. Hot Jupiters are expected to have strong CO features in the near-infrared but the Spitzer photometric bandpasses are about 1μm wide and cover spectral features from multiple different absorbing species. Several results from Spitzer suggest absorption from carbon-bearing species but it is challenging to unambiguously identify the kind of absorber present (Désert et al., 2009; Stevenson et al., 2010; Madhusudhan et al., 2011; Morley et al., 2017). The only definitive detections of CO are from high-resolution ground based spectroscopy (e.g. de Kok et al. 2013; Brogi et al. 2014).

Some noteworthy molecules have not yet been seen. These include NH_3 and CH_4 which are usually very abundant in the Solar System gas giants. But this is not a big surprise either since these molecules are unstable at high temperatures and will more likely be seen in cooler targets than hot Jupiters. Despite many searches, no definitive evidence for TiO/VO exists either (Sing et al., 2013; Evans et al., 2016). These molecules are expected in hot planets (Fortney et al., 2008), but they may rain out or get cold trapped deep in the atmosphere (Parmentier et al., 2013)

Abundances

Beyond detection, the strength of spectral features can be used to measure the atmospheric abundances of individual atoms that helps build a chemical inventory of the planet's atmosphere. Abundances are quantified in terms of their enrichment over the Solar value (i.e. the expected abundance for a Solar composition gas at the temperature of the planet's

atmosphere).

Spectra are useful in that they provide insights on an atmosphere's temperature profile, vertical mixing and bulk composition. By comparing the equilibrium expectations under the inferred temperature profile to the observed abundances, it is possible to infer disequilibrium chemistry and vertical mixing in exoplanet atmospheres, as has been done in the Solar System (e.g Prinn & Barshay 1977). Then, these spectra and inferred compositions can be used to compare different planets - called comparative exoplanetology. This is where exoplanet science can expand our general understanding of planet formation and evolution even if the measurements are far less comprehensive than for the Solar System planets.

Precise determinations of abundances are challenging, even if the molecular absorption is detected with high confidence. Just based on the transmission spectra, there are order of magnitude degeneracies between chemical mixing ratios and atmospheric pressure (Benneke & Seager, 2012; Griffith et al., 2013). This can be broken with the planet's thermal emission spectra, as they are more sensitive to absolute abundances. This is because the shape and amplitude of spectral features depend on the temperature pressure profile. For example, Stevenson et al. (2017) measured the water abundance for the hot Jupiter WASP-43b to better than a factor of five (0.3-1.7 $\times$ Solar at 1σ confidence).

Another technique to improve precision requires observations in multiple absorption bands for the same molecule in transmission (Benneke & Seager, 2012). Wakeford et al. (2017b) did detect two water features in the transmission spectrum of the warm Neptune HAT-P-26b and retrieved a water abundance of $4.8^{+21.5}_{-4.0}$ $\times$ Solar. Even though these are much less precise than what we have for Solar System planets, there is a much larger and more diverse sample of exoplanets available to study. Thus, a dedicated atmosphere characterization mission could measure abundances for hundreds of planets, and provide a complementary test of planet formation models that could add to studies done for the Solar System (Chapman et al., 2017).

If the chemical reaction timescale is long in comparison to horizontal/vertical mixing timescale, chemical reactions cannot happen fast enough while the gas is transported from one side to the other and quenching happens. Atmospheric circulation can then drive the chemical abundances out of their local equilibrium state and erase any chemical gradient expected from local equilibrium (Cooper & Showman, 2006; Visscher & Moses, 2011). A combination of chemical equilibrium abundances of deep atmosphere (vertical quenching) and of hot dayside (horizontal quenching) determines the exact chemical composition of the atmosphere (Agúndez et al., 2014). Chemical quenching is expected to affect opacities

in very specific bands, leading to a peculiar signature in the day/night contrast versus wavelength relationship (Steinrueck et al., 2018).

In the case of very hot planets ($T_{eq} \geq 2500$K), molecules such as water should be thermally dissociated in the dayside photosphere but not in the nightside, whereas molecules like CO that have stronger bonds should be present at all longitudes. When molecules dissociate, continuum opacities from hydrogen ions are expected to become dominant, leading to less spectral features and blackbody like thermal emission in the dayside (Kreidberg et al., 2018; Arcangeli et al., 2018)

In our Solar System, we have a pattern of increasing atmospheric metallicity with decreasing planet mass - from a factor of few enhanced over Solar for Jupiter to $\sim$ 100 times Solar for Uranus. Planet population synthesis models this trend naturally, as they show that lower mass planets are relatively more polluted by infalling planetesimals (Mordasini et al., 2016; Fortney et al., 2013). If we use water as a tracer for metallicity, we see that WASP-43b agrees well with the Solar System patterns but HAT-P-26b is less enriched than expected, demonstrating the diversity of atmospheric compositions. For the Solar System gas giants, the water abundances are poorly constrained since water is condensed deep in their atmospheres (Showman & Ingersoll, 1998; Mousis et al., 2014).

1.4.2. Climate

A planet's climate can be characterized in detail with the help of thermal emission measurements. These observations have focused largely on hot Jupiters because of their large planet-to-star flux ratios. The most common measurement is of dayside brightness temperature that has been inferred from secondary eclipse observations for over 50 planets (Schwartz & Cowan, 2015), and they range from about 1000 to 3000 K (Stevenson et al., 2014a; Kammer et al., 2015; Morley et al., 2017).

Thermal Inversions

Fortney et al. (2008) predicted two classes of hot Jupiter atmospheres - those with thermal inversions (temperatures increasing with height) and those without. It turns out that the dividing factor is whether gaseous TiO/VO are present in the atmosphere. These molecules are very strong optical absorbers and significantly heat the upper atmosphere even when present in trace amounts. They are only expected to be present in the hottest atmospheres with fluxes greater than 10^9 erg s^{-1} cm^{-2}, since at cooler temperatures they

will condense and rain out of the atmosphere.

The hot Jupiter HD 209458b falls on the dividing line between the two classes. Early Spitzer observations suggested that its atmosphere has a thermal inversion (Knutson et al., 2008). But new data showed this was not the case and that the temperature profile was actually decreasing with height (Diamond-Lowe et al., 2014; Schwarz et al., 2015; Line et al., 2016). More recently, evidence has been found for weak inversions (isothermal profiles) in the atmospheres of other planets (Stevenson et al., 2014b; Haynes et al., 2015), each one of which has an extremely hot dayside temperature, greater than 2500 K. That suggests that temperature does play a role in determining the thermal structure.

Global Heat Circulation

Thermal phase curves in infrared wavelengths provide insights into the global climate. The first phase curve that was measured was for the hot Jupiter HD 189733b with Spitzer by Knutson et al. (2007b). They measured a small difference of 250 K in temperature between the dayside and the nightside and an offset in the peak brightness to the east of the substellar point. These results are in agreement with expectations from 3D Global Circulation Models that predict efficient heat redistribution for slower rotation period, and eastward equatorial jets caused by the interaction of Rossby waves with the planet's rotation (Showman et al., 2009).

The first spectroscopic phase curve was for the hot Jupiter WASP-43b with HST's WFC3 instrument (Stevenson et al., 2014b). Since these phase curves are multiwavelength, they were sensitive to a range of pressure levels in the atmosphere which enabled a determination of the planet's thermal structure as a function of longitude and altitude. It was estimated that the planet has a low Bond Albedo (0.2) a large day-night temperature contrast (suggesting the presence of clouds on the nightside) and a hotspot that is shifted further east at higher pressures, indicative of a more efficient heat transport deeper in the atmosphere. A Spitzer phase curve for the super-Earth (2 Earth Radii) 55 Cancri e (Demory et al., 2016) was the first phase curve measured for a small planet. The measurement revealed a dayside temperature of 2700K, with a 1300K drop in temperature on the nightside. There is a large hotspot offset of about 40 degrees east of the substellar point. The results are consistent with either molten rock on the dayside, or an optically thick atmosphere with minimal heat redistribution.

1.4.3. Condensates - Clouds and Hazes

Condensates are ubiquitous in the Solar System planet atmospheres and are now very commonly found in exoplanets as well. About half of the hot Jupiters show evidence for condensates in their spectra (Sing et al., 2016). Due to the slant viewing geometry observed during transit, transmission spectra are particularly sensitive to the presence of condensates (Fortney, 2005).

Condensates have three main effects on transmission spectra. First they block the stellar flux from transmitting, effectively truncating spectral features below the cloud-deck height. Second, they can also introduce a slope in the spectrum over wavelength intervals of several microns (Sing et al., 2016). The third effect is scattering off of cloud and haze particles at optical wavelengths, which introduces a steep increase in the transit depth towards the blue (Pont et al., 2008)

The first hint of condensates being present in extrasolar planet atmospheres came from HD 209458b that showed a smaller than expected Na feature relative to a clear atmosphere (Charbonneau et al., 2002). This observation was followed by a slew of spectra with truncated features (e.g. Deming et al. 2013; Crossfield et al. 2013; Kreidberg et al. 2014b; Knutson et al. 2014; Kreidberg et al. 2015).

Many spectra also show the large optical slope indicating scattering from small particles (e.g. Lecavelier Des Etangs et al. 2008a; Sing et al. 2011b, 2013; Robinson et al. 2014; Dragomir et al. 2015). Transit depth offsets between 1 and 5 μm were also seen in many hot Jupiters (Sing et al., 2016).

There are several indirect constraints on condensate properties. Optical phase curves of hot Jupiters, for example, are best explained by reflective clouds on their western hemispheres, composed of silicate and manganese sulfide (Demory et al., 2013; Oreshenko et al., 2016; Parmentier et al., 2016). Amplitude of spectral features gives further clues - the spectrum of the super-Earth GJ 1214b is featureless at high precision (30ppm, Kreidberg et al. 2014b). Truncating the features to this extent requires an optically thick condensate layer at a pressure level of 0.1 millibar which can be achieved either by thick, lofted clouds or very efficient haze formation (Morley et al., 2015).

1.5. Gaps and Challenges

Despite the body of evidence for condensates in atmospheres of hot Jupiters, the compositions of condensates remains elusive! Many theoretical possibilities exist, including

equilibrium condensates such as water, salt, sulfide or silicate clouds (depending on temperature) and photochemical hazes like hydrocarbon soots formed from photolyzed methane (Burrows & Sharp, 1999; Miller-Ricci Kempton et al., 2012; Morley et al., 2013; Wakeford et al., 2017a). Current transmission spectra lack the wavelength coverage and precision needed to distinguish between these species in exoplanets. In brown dwarfs, a silicate feature at 9 μm has been tentatively detected using Spitzer/IRS (Cushing et al., 2006). Future observations of exoplanets could also reveal features from specific grains, which would unambiguously determine their composition (Wakeford & Sing, 2015).

There is some evidence that condensates are more prevalent at lower temperatures (Stevenson, 2016; Heng, 2016). However, the microphysics of condensate formation are complex and depend sensitively on the thermal structure and circulation of the atmosphere (Turco et al., 1979). More atmosphere studies are needed to determine whether the presence of condensates can be predicted from temperature or other basic properties.

Observations of thermal phase curves of hot Jupiters show that in general they have a large amplitude (between 0.5 to 1) and an eastward offset. There is no clear trend between the amplitude of thermal phase curves and planet equilibrium temperature. Earlier claims by Perez-Becker & Showman (2013) and Komacek & Showman (2016) were based on a smaller number of observations and a combined interpretation of observations taken in different bandpasses. But in today's more complete datasets, no trend is visible.

Another tentative trend, as first proposed in Stevenson et al. (2017), can be seen between amplitude versus planet rotation period - planets with a faster rotation rate have larger phase curve amplitude. A large offset is expected when the planet temperature is higher, but according to the current trends the phase curve offset versus equilibrium temperature plot shows a lack of a large offset for planets with equilibrium temperatures $\geq$ 1700 K. Even then, super-Earth 55 Cnc e does not fit in this trend of hot Jupiters, and its phase curve appears similar to cooler hot Jupiters like HD 209458b that have a large offset and a large phase curve amplitude at 4.5μm that points towards unique atmospheric properties.

We can begin to understand energy balance in terms of the amount of incoming energy reflected to space (Bond albedo) and the amount of absorbed stellar light that is transferred to the nightside (Redistribution Factor). Ideally, in order to obtain a complete energy balance, the full dayside and nightside spectra should be used. But current observations only cover a few bandpasses and the effective temperature of each hemisphere must be estimated by extrapolating the measurements with the assumptions of a blackbody emission. These can work for the planet's dayside (Cowan & Agol, 2011a) but might fail

for the nightside because the vertical temperature gradient is larger (Schwartz & Cowan, 2015). Later results from Schwartz et al. (2017) show no trends between equilibrium temperatures and day/night temperature contrast along with a large dispersion in both the redistribution efficiency and the geometric albedo between planets. Schwartz et al. (2017) also show that many hot Jupiters have Bond albedos larger than 0.3 which is in direct contradiction with their measured low geometric albedos in the Kepler bandpass (Heng & Demory, 2013). This discrepancy, called the hot Jupiter Albedo Problem could be due to the asymmetric scattering function (Dyudina et al., 2005), a lower geometric albedo in the Kepler bandpass than outside of it (Crossfield, 2015) or an intrinsic bias in the method.

If we need to link the phase curve amplitude and the phase offset, it will require a model for the longitudinal distribution of the temperature and the opacities. One/two dimensional models of longitudinal/latitudinal variations of the temperature have been calculated by taking into account the competing effects of the longitudinal advection of energy and the radiative losses (Cowan & Agol, 2011b; Hu et al., 2015; Zhang & Showman, 2017). They make temperature maps that are determined by the ratio of advective and radiative timescales. Consequently, they always predict a correlation between the phase curve offset and the amplitude. But they neglect the vertical transport, which is an important factor that sets the day/night temperature contrasts (Komacek & Showman, 2016). The phase curve offset and amplitude might then be actually set by different mechanisms, which could be the reason why they are not correlated in the observations (Crossfield, 2015) nor in the more complex, three-dimensional models of tidally locked exoplanets (Komacek et al., 2017; Parmentier et al., 2016).

The phenomenological models described above are useful to retrieve parameters such as the radiative timescale from phase curve observations but they really cannot define the mechanisms that are setting these parameters. For this purpose, Global Circulation Models (GCM) have been used in order to quantitatively link the observed day/night contrast and phase curve offset to planetary parameters. They solve for the hydrodynamics, radiative transfer and/or magnetic effects in three dimensions. When trying to match observations to the predictions of GCMs, we see that cloudless, dragless, Solar composition models systematically underpredict the amplitude and over predict the offset of thermal phase curves (Showman et al., 2009; Kataria et al., 2015). Other mechanisms like metallicity (Kataria et al., 2015), cloud composition (Oreshenko et al., 2016; Parmentier et al., 2016), rotation period (Showman et al., 2009; Showman & Polvani, 2011), disequilibrium chemistry (Cooper & Showman, 2006) and the magnetic field strength (Rogers, 2017) must be an important part of the description.

The radiative timescale is expected to vary linearly with pressure and with the inverse cube of the temperature (Iro et al., 2005; Showman et al., 2008). The pressure dependence of the radiative timescale has major consequences on the observations, because the pressures probed span several orders of magnitude. At wavelengths probing deep in the atmosphere, the phase curves obtained are expected to show a large radiative timescale, a small amplitude and a large offset. Conversely, phase curves obtained at wavelengths probing shallower layers (e.g. inside molecular bands) showed a larger amplitude and smaller offset. The temperature dependence of the radiative timescale is also expected to impact the observations. If other things are kept equal, hotter planets are expected to cool more efficiently leading to a larger day/night temperature contrast and thus a larger phase curve amplitude (Perez-Becker & Showman, 2013; Komacek & Showman, 2016). But a lack of clear trend in the amplitude versus equilibrium temperature plot indicates that other mechanisms must contribute to the shape of the exoplanet's phase curves (Komacek et al., 2017).

For planets with equilibrium temperatures greater than 1900 K, titanium and vanadium oxides are expected to be present in the dayside atmosphere and create a strong thermal inversion (Hubeny et al., 2003; Fortney et al., 2008; Parmentier et al., 2015, 2016). The detection of such an inverted temperature profile has recently been claimed through the presence of molecular emission features in the dayside of both WASP-33b (Haynes et al., 2015) and WASP-121b (Evans et al., 2017). Thermal inversions are expected to disappear in the planet's nightside where these molecular features are expected to become absorption features.

Clouds strongly impact transit spectra because longer optical path lengths permit a greater sensitivity to trace cloud species. To date, only 1D limb averaged cloud models have been used to interpret transmission spectra but the presence of inhomogeneous clouds along the terminator can influence our interpretation of the transit spectra. Line & Parmentier (2016) performed retrievals on a synthetic Solar composition hot Jupiter with patchy clouds and a cloud-free high mean molecular weight warm Neptune. They concluded that there exists a degeneracy between the two cases, i.e. both cloud-free high mean molecular weight atmospheres and partially cloudy atmospheres can explain the data equally well.

Another key finding is that the HST/WFC3 transmission spectra of two well-observed objects, the hot Jupiter HD 189733b and the warm Neptune HAT-P-11b, can be well explained well by Solar composition atmospheres with patchy clouds without the need to invoke high mean molecular weights or global clouds. The degeneracy between high molecular weight and partially cloudy Solar composition atmospheres can be broken by observing the molecular Rayleigh scattering differences between the two. Furthermore, the

signature of partially cloudy limbs also appears as a $\sim$ 100 ppm residual in the ingress and egress of the transit light-curves, provided that the transit timing is known to seconds.

The current sample shows that every exoplanet studied so far is unique in many of their properties. Many more such gaps and questions exist in our understanding of exoplanetary atmospheres. Due to technological and time limitations, one has only begun to scratch the surface.

1.6. This Thesis

For the specific purpose of this thesis, we focus on working with one hot Jupiter, namely WASP-43b. We have discussed many of the open questions regarding its properties above, but we now focus on the hot Jupiter Albedo Problem. We present the full reflection spectra of WASP-43b, where the data was obtained using HST and TESS as described in the article that follows. We measured optical eclipse depths, and determined the corresponding geometric albedo values. We also determine the spectroscopic geometric albedo measurements by binning the white light in different wavelength bins. We make inferences for atmospheric properties as exhibited by our best fitting models and compare with the previously published simulations and our own models.

1.6.1. Contributions of the Author

My main contributions to the article presented in the next chapter were the reduction and the complete analysis of the data obtained, implementation of the Gaussian Process framework into the ExoTEP pipeline and redaction of the complete article for publication. WASP-43b was observed by Björn Benneke as a part of a collaboration comprised of the coauthors. Our atmosphere models used for discussion were produced by J. K. Barstow. I also wrote the entire thesis presented here, created the figures and tables with the exception of the figures presented in the introduction that I simply adopted from the references mentioned therein.

Chapter 2

The curious case of WASP-43 b: First full reflective spectra using HST and TESS

Prashansa Gupta[1,2], Björn Benneke[1,2], Joanna K. Barstow [3], Nicolas B. Cowan[4,5], Ian J. M. Crossfield[6,9], Travis S. Barman[7], Neale P. Gibson[8], Thomas M. Evans[9], Nikolay Nikolov[10], David K. Sing[11], Heather A. Knutson[12], Tiffany Kataria[13], Joshua D. Lothringer[14], Joel C. Schwartz[5]

[1] *Institut de recherche sur les exoplanètes* [2] *Département de physique, Université de Montréal, Montréal, QC H3C 3J7, Canada*

[3] *Department of Physics and Astronomy, University College London, Gower Street, London WC1E 6BT, UK*

[4] *McGill Space Institute, 3550 rue University, Montreal, QC, H3A 2A7, Canada*

[5] *Department of Physics, McGill University, 3600 rue University, Montréal, QC H3A 2T8, Canada* [6] *Department of Physics, Massachusetts Institute of Technology, 77 Massachusetts Ave, Cambridge, MA, 02139, USA*

[7] *Lunar and Planetary Laboratory, University of Arizona, 1629 E. University Boulevard, Tucson, AZ 85721, USA*

[8] *Astrophysics Research Centre, School of Mathematics and Physics, Queens University Belfast, Belfast BT7 1NN, UK*

[9] *Kavli Institute for Astrophysics and Space Research, Massachusetts Institute of Technology, 77 Massachusetts Avenue, 37-241, Cambridge, MA 02139, USA*

[10] *Department of Physics & Astronomy, Johns Hopkins University, Baltimore, MD, USA*

[11] *Department of Earth and Planetary Sciences, Johns Hopkins University, Baltimore, MD, USA*

[12] *Division of Geological and Planetary Sciences, California Institute of Technology, Pasadena, CA 91125, USA*

[13] *NASA Jet Propulsion Laboratory, 4800 Oak Grove Drive, Pasadena, CA 91109, USA*

[14] *Lunar and Planetary Laboratory, University of Arizona, 1629 E. University Boulevard, Tucson, AZ 85721, USA*

To be submitted to *The Astrophysical Journal*

Abstract

We present for the first time the full reflection spectra for the well-characterized hot Jupiter WASP-43b in the 290-1000 nm waveband using the Space Telescope Imaging Spectrograph (STIS) onboard the Hubble Space Telescope (HST) and the Transiting Exoplanet Survey Satellite (TESS) mission. These measurements allow us to constrain the planet's geometric albedo to $-0.11^{-0.17}_{+0.18}$ in the HST/STIS 290-570 nm waveband and to 0.11 ± 0.03 in the TESS 600-1000 nm waveband . Further binning into two, four and six wavelength bins of equal flux across the HST/STIS wavelength range also produces limits over spectroscopic geometric albedo values, which show a potential increase in the geometric albedo towards shorter wavelengths. We use these eclipse depth limits to further test and compare the previously determined atmospheric models for this planet. We find that WASP-43b favours a cloudy atmosphere with $1\mu m$ Enstatite particles and 10 times the Solar Na abundance. The lack of visible-wavelength reflection data for the best characterized hot Jupiters is a gaping hole in our current understanding of exoplanet atmospheres as the UV+optical albedo spectrum contains information unavailable at other wavelengths. This dataset will therefore prove to be a milestone, complementing the upcoming observations with the James Webb Space Telescope that will not be able to observe in the HST UV-optical wavelength regions.

Keywords: planets and satellites: atmospheres - stars: individual (WASP-43)-techniques: photometric

2.1. Introduction

Various searches for reflected light from hot Jupiters through broadband photometry from Kepler, CoRoT and MOST telescopes in the past, have indicated that hot Jupiters typically have low geometric albedos ($A_G(\lambda)$, the wavelength dependent reflectance) at optical wavelengths ($A_G \leq 0.1$; e.g Rowe et al. (2008); Kipping & Spiegel (2011); Heng & Demory (2013); Dai et al. (2017)) where the host star emits most of its energy. However, thermal emission measurements (mostly obtained from the Spitzer Space Telescope) suggest that hot Jupiters' Bond Albedo (A_B, the bolometric ratio of emitted vs incident power) are typically $A_B \sim 0.4$ (Schwartz et al., 2017). This apparent discrepancy between constraints from thermal and optical measurements points towards a gaping hole in our understanding of exoplanet atmospheres.

In an attempt to explain this discrepancy, an eclipse observation of HD 189733b was obtained using the Hubble Space Telescope's (HST) Space Telescope Imaging Spectrograph (STIS) instrument (Evans et al., 2013). This dataset showed an increase in reflectivity towards the bluer wavelengths which may partly explain the problem. Following this, a

second set of observations for a much hotter WASP-12b were published (Bell et al., 2017). Their results were in stark contrast as they showed very low albedo values implying a much darker planet. The fact that the first two exoplanets with spectrally resolved reflected light observations exhibit significant differences, directly points to the importance of investigating the reflective spectrum of exoplanets.

We present the reflective spectrum of the third exoplanet in this series, WASP-43b. One of the closest orbiting hot Jupiters with twice the mass and roughly the same size as Jupiter, WASP-43 b was discovered in 2011 (Hellier et al., 2011) and is located in the constellation of Sextans. WASP-43 b orbits a relatively cool K7 star (4520 ± 120 K) of mass $0.73 M_{\odot}$ (Gillon et al., 2012). It has the smallest semi-major axis of all confirmed hot Jupiters and one of the shortest orbital periods (0.01526 AU and 19.5 h respectively, Gillon et al., 2012) properties that make it an excellent target to observe in transit. The planet is also a good candidate for eclipse and phase curve observations due to the important flux ratio between emission of the star and the exoplanet.

To date many observations of the planet's atmosphere have been conducted from the ground. The only ground-based eclipse observations that exist are from Wang et al. (2013), who observed WASP-43b in the H and the K_s bands with the CFHT/WIRCam instrument and published eclipse depths of 1030 ± 140 ppm and 1940 ± 290 ppm respectively. However, many more ground-based transit observations have been obtained in the optical-nearIR-IR wavebands. Gillon et al. (2012) observed nearly two dozen ground-based transit light-curves to improve the precision of the system parameters and reported a high confidence detection of the nightside thermal emission of 1560 ± 140 ppm at $2.09 \mu m$, while Chen et al. (2014) reported a K-band detection of 1970 ± 420 ppm. Although generally consistent with each other, ground based observations are inconsistent with high precision space observations, as they may tend to over-predict measured eclipse depths in lower-quality light-curves due to unexplained or under-modeled systematics (Rogers et al., 2013). Murgas et al. (2014) obtained transit observations in the red-optical that showed weak excess in R_p/R_s near the Na I doublet and a smoothly varying trend at redder wavelengths. While both Blecic et al. (2014) and Murgas et al. (2014) constrained the tidal decay rate, Ricci et al. (2015), with seven additional transit timing constraints, found no evidence of orbital decay.

From space, using the Spitzer Space Telescope, Blecic et al. (2014) measured dayside emission at $3.6 \mu m$ and 4.5 μm, ruling out the presence of a strong thermal inversion and suggesting a low day-night heat redistribution. Stevenson et al. (2014b) published spectroscopic thermal emission phase curve measurements with HST/WFC3 confirming low day-night heat redistribution in stark contrast with the modest day-night differences inferred from Spitzer photometric phase curves of similarly irradiated giant planets (Perez-Becker & Showman, 2013). Kreidberg et al. (2014a) determined a precise water abundance consistent with a Solar composition and a metallicity matching the trend of Solar System giant

planets. Kataria et al. (2015) presented 3D atmospheric circulation models that required the existence of thick, high altitude clouds on the nightside. They also concluded that a 5 times Solar metallicity model matches the dayside emission spectrum and that the planet exhibits equatorial superrotation. In Stevenson et al. (2017), three full-orbit broadband photometric phase curves were obtained with Spitzer at $3.6\mu m$ and 4.5 μm. Though consistent with Blecic et al. (2014), they showed weak evidence for variability and the nightside flux inconsistency remained a mystery. However, by demanding non-negative brightness maps while phase curve parameters are fit simultaneously with astrophysical and detector noise sources, Keating & Cowan (2017) showed that WASP-43b may no longer be an outlier with inexplicably low day-night heat transport and that the models of Kataria et al. (2015) may not be missing crucial physics after all.

Although secondary eclipses for WASP-43b have been observed previously at infrared wavelengths, our new observation is the first measured at short wavelengths where thermal emission from the planet is negligible. Thus, any light detected is entirely due to scattering in the atmosphere, which can be used to place unambiguous constraints on the geometric albedo A_g according to,

$$A_g = \delta \left(\frac{R_p}{a}\right)^{-2}, \tag{2.1.1}$$

where δ is the fractional eclipse depth, R_p is the planet radius and a is the orbital semi-major axis. This equation follows from the formal definition of A_g. i.e. the observed flux of scattered light at full phase divided by the flux that an isotropically scattering disk with the same cross-sectional area would have if it were placed at the same location as the planet (Seager, 2010).

We observed the planet in eclipse using the HST/STIS instrument three times, and report the white light eclipse depths with the corresponding geometric albedo. We then bin the white light observations into two, four and six wavelength bins, and report on the corresponding geometric albedo spectrum. We also fit the eclipse light-curve observed by TESS and report on the eclipse depth and the corresponding geometric albedo. For the analysis, we add the Gaussian Process technique into the ExoTEP framework, and compare its fits with the traditionally used fourth order polynomial as the systematics model. We also employ an exponential time ramp, instead of the widely used linear function to fit the HST/STIS datasets. Lastly, we compare our results with atmospheric models provided by our NEMESIS code simulations and previously published atmospheric models.

We describe the observations and data reduction methodology in Section 2.2. In Section 2.3, we discuss the analysis methodology for the light-curves, and the results obtained follow in Section 2.4. We conclude with a discussion in Section 2.5.

2.2. Observations and Data Reduction

2.2.1. HST Spectroscopy

As part of the program GO-14797 (PI: Ian Crossfield), three eclipses of WASP-43b were observed using the STIS G430L grism on HST in the wavelength range 290 to 570 nm on 2016 October 27, 2017 March 15, and 2017 June 15, hereafter termed as visits 1, 2 and 3 respectively. Each visit is comprised of four HST orbits, out of which the first orbit is discarded from the analyses. This is because the spectra taken during the first orbit exhibited much worse systematics than those taken in subsequent orbits, a feature that can be attributed to the settling of the telescope into its new pointing position. Out of the remaining three orbits, the first and the third sampled the out-of-eclipse flux when both planet and star were visible with planet near full phase (star plus planet), while the second sampled the in-eclipse flux when the planet was fully obscured by the star (star only). Each visit consists of four 96-minute telescope orbits, with 48-minute gaps in phase coverage between target visibility periods due to Earth occultation.

We follow the same data collection method as done previously for similar observations (Sing et al., 2011b, 2013, 2016; Evans et al., 2013). The G430L grating has a resolution R of $\lambda/\Delta\lambda = 530 - 1{,}040$ (~ 2 pixels; 0.55 nm). The observations were taken in subarray readout mode with a wide $52'' \times 2''$ slit to minimize time-varying slit losses caused by pointing drifts and reduced overheads by reading out only 1024×128 pixel subarray containing the target spectrum. Previous HST/STIS experience informed us that the first exposure of each HST orbit had systematically lower counts than the ones that followed, so a 1 s dummy exposure was taken at the beginning of each orbit followed by 10 science exposures lasting 279 s each (the maximum recommended duration to avoid excessive cosmic ray impacts). Our final dataset thus consisted of three visits, each with 30 exposures collected over 240 minutes.

This raw STIS dataset was reduced using the latest version of the `CALSTIS1` pipeline and the relevant up-to-date calibration frames that includes bias-, dark-, and flat-corrections and cosmic ray removal. Next, the IRAF apall routine was used to extract the spectra from the calibrated .flt science files. To determine the appropriate aperture, we tested for aperture values between 10.0 and 25.0 pixels in intervals of 2.0 pixels. We found that a 20.0 pixel aperture resulted in the lowest light-curve residual scatter after fitting the white light data. We then carried out a cross-correlation to correct for subpixel shifts along the dispersion axis. The x1d files from `CALSTIS1` were then used to calibrate the wavelength axis. Finally, both the 'white light' and the two, four and six spectral channel light-curves were produced by integrating the appropriate flux in each bandpass.

Separate analyses were performed for a two-channel, four-channel and six-channel binning: Figure 2.1 shows the median 1D stellar spectrum with the adopted six-channel wavelength bins overplotted and Table 2.1 explicitly lists the wavelength ranges.

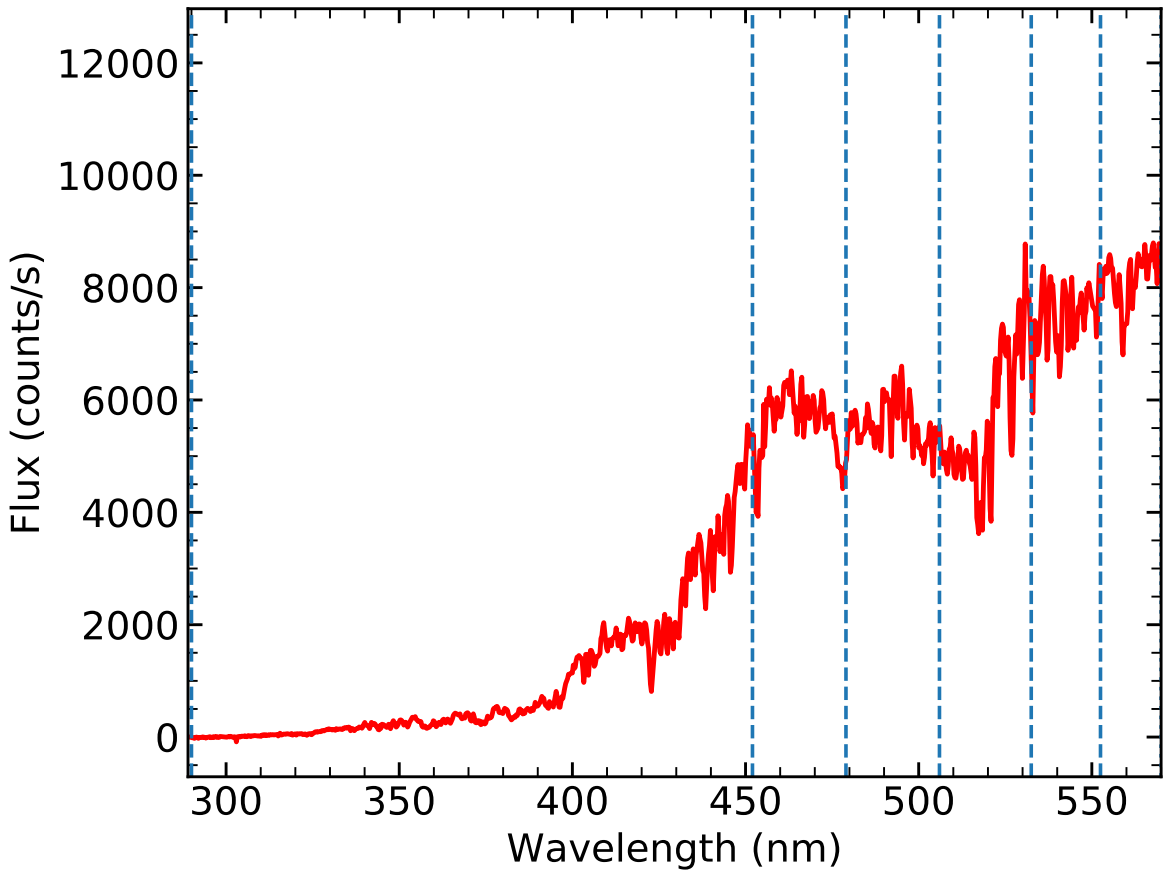

Fig. 2.1. The median 1D stellar spectrum is shown in red. Also shown are the boundaries of the six wavelength bins as dotted blue lines.

2.2.2. TESS Photometry

WASP-43, listed in the TESS Input Catalog (TIC; Stassun et al. 2018) as TIC 36734222, was photometrically monitored by TESS for 25 days from February 28 to March 25 2019 in sector 9, year 1 of its primary mission. This data was processed with the Science Processing Operations Center (SPOC) pipeline (Jenkins et al., 2016) hosted at the NASA Ames Research Center that is mostly based on the predecessor Kepler mission pipeline (Jenkins et al., 2010, 2017)

After downloading the data from the Mikulski Archive for Space Telescopes (MAST), we proceeded to analyze the light-curves using methodologies largely identical to previous TESS papers (Shporer et al., 2019; Wong et al., 2019). We employed the Presearch Data Conditioning (PDC, Smith et al. 2012; Stumpe et al. 2014) light-curves from the SPOC pipeline, which have been corrected for instrumental systematics and contamination from nearby stars. There was very little stray light contamination on the detector, and the SPOC pipeline flagged these exposures and set the fluxes as NaN. So we removed all the flagged

Table 2.1. Eclipse Depths and Geometric Albedo Measurements for WASP-43b

Bins	**Wavelengths** (nm)	**Eclipse Depth** δ (ppm)	**Geometric Albedo** A_g
		HST	
White	290-570	-120^{-180}_{+190}	$-0.11^{-0.17}_{+0.18}$
2	290-505	300^{-270}_{+270}	$0.28^{-0.26}_{+0.26}$
	505-570	-110^{-210}_{+200}	$-0.10^{-0.20}_{+0.19}$
4	290-465	790^{-380}_{+360}	$0.75^{-0.36}_{+0.34}$
	465-505	-320^{-300}_{+290}	$-0.30^{-0.28}_{+0.26}$
	505-542	-60^{-280}_{+250}	$-0.06^{-0.27}_{+0.24}$
	542-570	10^{-30}_{+27}	$0.01^{-0.03}_{+0.03}$
6	290-452	1200^{-470}_{+430}	$1.14^{-0.45}_{+0.41}$
	452-479	260^{-250}_{+250}	$0.25^{-0.24}_{+0.24}$
	479-506	-640^{-360}_{+360}	$-0.61^{-0.34}_{+0.34}$
	506-532	330^{-260}_{+270}	$0.31^{-0.25}_{+0.26}$
	532-552	-340^{-300}_{+300}	$-0.32^{-0.28}_{+0.28}$
	552-570	-40^{-290}_{+310}	$-0.04^{-0.28}_{+0.29}$
		TESS	
White	600-1000	111^{-34}_{+33}	$0.11^{-0.03}_{+0.03}$

data points from the light-curve. The resulting light-curve has a photometric precision of roughly 1500 ppm and contains 27 transits and 28 secondary eclipses of WASP-43b.

2.3. Light Curve Analysis

We analyze the HST/STIS light-curves in the ExoTEP framework, to which we add our homemade Gaussian Process (GP) code. We also compare the GP analysis to the traditional fourth order polynomial method. We also attempt to model time dependence of instrumental effects using an exponential ramp instead of the widely used linear function based on empirical data, but in the end find consistent eclipse depths.

Figure 2.2 shows eclipse fits in three panels for the three HST/STIS visits. The top panel in each visit shows the raw light-curve spanning the entire STIS G430L bandpass i.e. 'white light'. Each light-curve consists of three HST orbits and within each one of these, the measured flux shows a dominant, approximately repeatable, trend in flux. Visits 1 and 3 show an in-orbit decrease of $\sim$ 5000 ppm, while Visit 2 is peculiar in shape with a in-orbit fluctuation of $\sim$ 2500 ppm in relative flux. This is in addition to a longer term change in the baseline flux level. Visits 1 and 3 show a systematic decrease over time while Visit 2 shows an increase in relative flux. These systematics are believed to be primarily caused by the thermal cycle of HST throughout its orbit as well as to the drift of the spectral trace across the detector (Brown et al., 2001; Sing et al., 2011b; Huitson et al., 2012; Evans et al., 2013; Bell et al., 2017).

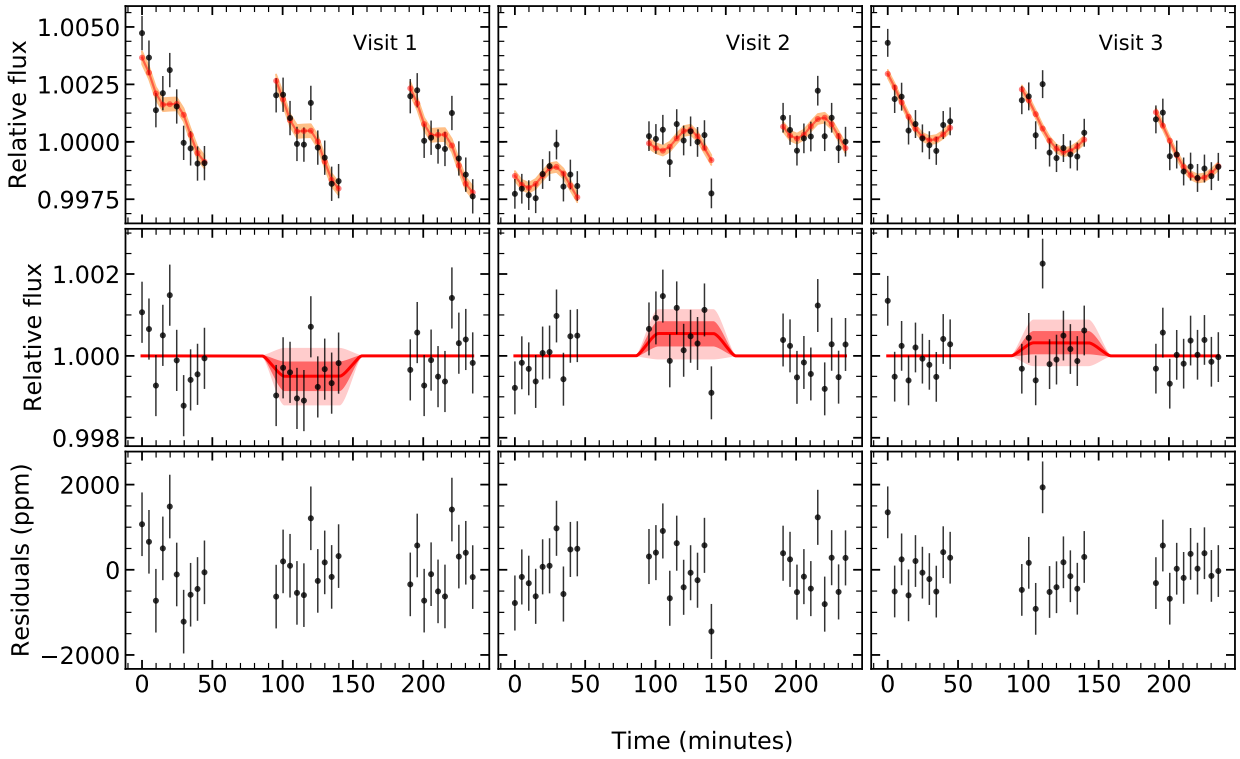

Fig. 2.2. Best fit eclipse light-curves for the three visits. The top panel for each visit shows the median normalized raw white light flux measurements (black dots) with the median systematic model (red line) and 1σ uncertainty (orange shading). The middle panels show the corrected flux measurements (black dots), overplotted with the best fit eclipse model (red line). The fluxes show variation about the out-of-eclipse baseline level normalized to 1.0. The red and light red shading mark the 1 and 2 σ uncertainty in the model respectively. Bottom panels show the residuals on ppm scale. The time begins with the first observation taken into account for analysis. All error bars only show uncorrelated white noise.

The standard approach in removing systematic trends is to model them with polynomial variations as a function of auxiliary variables (e.g. Sing et al. 2008a, 2011b; Huitson et al. 2012). But, model-dependent methods are only as accurate as the physics and assumptions included in the model. A polynomial fit may potentially lead to overfitting of the in-orbit variations, and thus bias the eclipse depth estimates. More recently, the exoplanet community has begun to explore model-independent methods of fitting by employing machine learning. Gibson et al. (2011) used the GP regression to model the HST systematics, followed by Evans et al. (2013). GPs introduce a Bayesian approach to effective estimation of eclipse/transit depths, robustly evaluating uncertainties and yielding results when there is insufficient data to support a rather complex fit. An in-depth discussion of modeling systematics with GPs can be found in Gibson et al. (2012a,b, 2013) and in Pass et al. (2019).

Our analysis framework is the Python-based Exoplanet Transits, Eclipses, and Phase Curves (ExoTEP) pipeline developed by B. Benneke (Benneke et al., 2017, 2019), which

handles everything from extracted raw photometry to transit parameters and their uncertainties as a single, statistically consistent Bayesian analysis. We jointly fit eclipse and systematics models along with photometric noise parameters using the Markov Chain Monte Carlo (MCMC) method. The main astrophysical output of the analysis is the eclipse depth (f_p) in the HST/STIS bandpasses.

2.3.1. Eclipse Model

The eclipse light-curve (here, named 'eclipse model') is implicitly calculated by ExoTEP using the `batman` implementation (Kreidberg, 2015) that is based on the equations derived in Mandel & Agol (2002). `batman` generates eclipse light-curves with

$$f = 1 - f_p(1 - \alpha), \tag{2.3.1}$$

where f is the normalized flux, f_p is the planet-to-star flux ratio and α is the fraction of the planet disk that is occulted by the star. The model is normalized such that the stellar flux is unity. For a separation d, the occulation fraction $\alpha(d) = \alpha_t(d)/R_p^2$, where $1 - \alpha_t(d)$ is the transit light-curve with uniform limb darkening. This model also assumes the planet flux is constant for all orbital phases.

2.3.2. Instrument Model

Phenomena such as the temperature settling of the telescope and the reinitialization of the read-out sequence at the beginning of each orbit manifest themselves as visit-long and orbit-long systematic trends. The visit-long trends can be modeled with a time dependent function, while the orbit-long systematics can be handled using polynomial or GP methods.

2.3.2.1. *Time Ramp*

For our time-dependent instrument model that should model visit-long time variations of the baseline flux, we use the standard procedure as described in many of the previous studies, of using a linear time ramp such as,

$$S(t) = c + vt, \tag{2.3.2}$$

where c and v are the normalization constant and the visit-long linear slope respectively, and t is the time since the beginning of the visit. We do not fit the c parameter in the case of GPs, but only for the polynomial fits.

The choice of the visit-long model will directly affect the determined eclipse depth. The linear time ramp has been employed for the case of HST data quite frequently, yet time series published in Demory et al. (2015) motivated us to pursue the exponential time ramp as well. This dataset observed previously with the same instrument demonstrates the accurate long term behaviour of the baseline flux when observed with HST. While trying to search for a

transiting planet, the authors observed α Centauri B for a total of 40 hours over two visits, one each in 2013 and 2014. A visual inspection of the time series reveals a clear non-linear increase in flux levels over the course of 16 orbits during the first visit, and 9 orbits in the second visit. This implies that the linear time ramp would only be an approximation to the actual exponential increase, for the case of a few orbits.

We fit this alpha Cen B dataset with our own two parameter exponential function as,

$$S(t) = ae^{(-t/\tau)} \tag{2.3.3}$$

where a is the amplitude of the time series, t is the time since the beginning of the observation and τ is the characteristic time constant that describes the rate of change of flux with time.

We estimated the characteristic time constant using this dataset and used it to further inform the fits for the WASP-43 b dataset. This technique yielded results consistent, within the uncertainties, with the linear time ramp model. Therefore, for a fewer number of HST orbits (three in our case of WASP-43b), the linear time ramp holds as a good approximation, but for a larger number of HST orbits, it would be neccessary to employ the exponential time ramp.

2.3.2.2. *Gaussian Process Model*

Instead of limiting possible fits to a single class of polynomial functions, the GP method, in contrast, does not assume any specific functional form, and thus is capable of fitting functions that are complex and unknown *a priori*.

Under the GP framework, the likelihood of a model is described as a multivariate normal distribution,

$$p(\boldsymbol{f}|\boldsymbol{\theta}) = \mathcal{N}(\boldsymbol{\mu}, \boldsymbol{K}) \tag{2.3.4}$$

where $\boldsymbol{f} = [f_1,...,f_N]^T$ are the N measured flux values, $\boldsymbol{\theta}$ are the model parameters, $\boldsymbol{\mu}$ is the model mean vector, $\boldsymbol{K}$ is the covariance matrix.

The 'eclipse model' as provided in Section 2.3.1 makes the $\boldsymbol{\mu}$ vector here. Off-diagonal entries of the covariance matrix $\boldsymbol{K}$ account for correlations between the measured flux and other variables that are unrelated to the eclipse signal, which we refer to as auxiliary variables. We used the squared exponential kernel to populate the entries of $\boldsymbol{K}$ such that:

$$K_{ij} = C^2 exp\left[-\Sigma_{d=1}^{D}\left(\frac{v_{d,i} - v_{d,j}}{L_d}\right)\right] + \delta_{ij}\sigma_w^2 \tag{2.3.5}$$

where C^2 is the covariance amplitude, $v_{d,i}$ and $v_{d,j}$ are the ith and jth values of the dth auxiliary variable, respectively, and L_d is the correlation length scale of the dth auxiliary variable.

In our case, we use the orbital phase of the HST ϕ as the auxiliary variable. This ϕ dependence accounts for the dominant systematic that repeats from orbit to orbit, while the

longer term change in the flux baseline will be accounted for by the linear (or exponential) time ramp independently. The δ_{ij} is the Kronecker delta function, which takes care of the white noise σ_w^2 in each measurement. This kernel then requires that the observations be strongly correlated if they have similar HST orbital phase, and this correlation dies out as one moves further away in covariate space. By parameterizing the covariance according to Equation 2.3.5, we are able to effectively model the poorly understood systematics as varying smoothly with respect to the auxiliary variables with the addition of white noise, without actually having to specify any functional form. Thus, our parameter set for the GP is $\boldsymbol{\theta} = [C^2, L_\phi, \sigma_W^2]$.

The standard method of fitting the orbit-long trends dictates the use of a fourth order polynomial of the form

$$S(t) = 1 + p_1 t + p_2 t^2 + p_3 t^3 + p_4 t^4$$

where p_1 to p_4 are coefficients that describe the systematic trends within each orbit. This method continues to be used extensively (Sing et al., 2008b; Nikolov et al., 2014; Sing et al., 2016; Wakeford et al., 2017b; Lothringer et al., 2018), but has very little physical significance. A fourth order (or higher) polynomial gives a greater ability to comfortably fit the systematics but also has the potential to overfit the data. This has direct consequences for the estimated eclipse depth.

The full set of parameters to model is then [f_p, v, C^2, L_ϕ, σ_w^2]. In order to explore every parameter and determine the most likely parameter values with their uncertainties, we use the Markov Chain Monte Carlo (MCMC) ensemble sampler software `emcee` (Foreman-Mackey et al., 2013). For computational reasons, we fit logarithms of all parameters except eclipse depth, since logarithms remove the need to use a prior to obtain strictly positive values. But for the case of eclipse depth, we allowed for negative values to obtain an unbiased estimate. To enable quick convergence within this high dimensional parameter space, ExoTEP first fits each transit light-curve individually and then automatically uses the best fitting systematics model parameters from the individual fits as initial conditions in the global MCMC fit.

We fit the WASP-43b dataset using this standard method and compare our results with the GP method. The Figure 2.3 illustrates this comparison among the white light eclipse depth fits. Within the uncertainties, the fourth order polynomial method is quite consistent with the GP method.

2.3.3. HST/STIS Eclipse Spectrum

The full reflection spectrum is obtained by performing independent fits to different spectral bins. As Figure 2.1 shows, there is very little incoming light at the shorter wavelengths, which implies that we expect higher uncertainties in the wavebins covering them. Therefore,

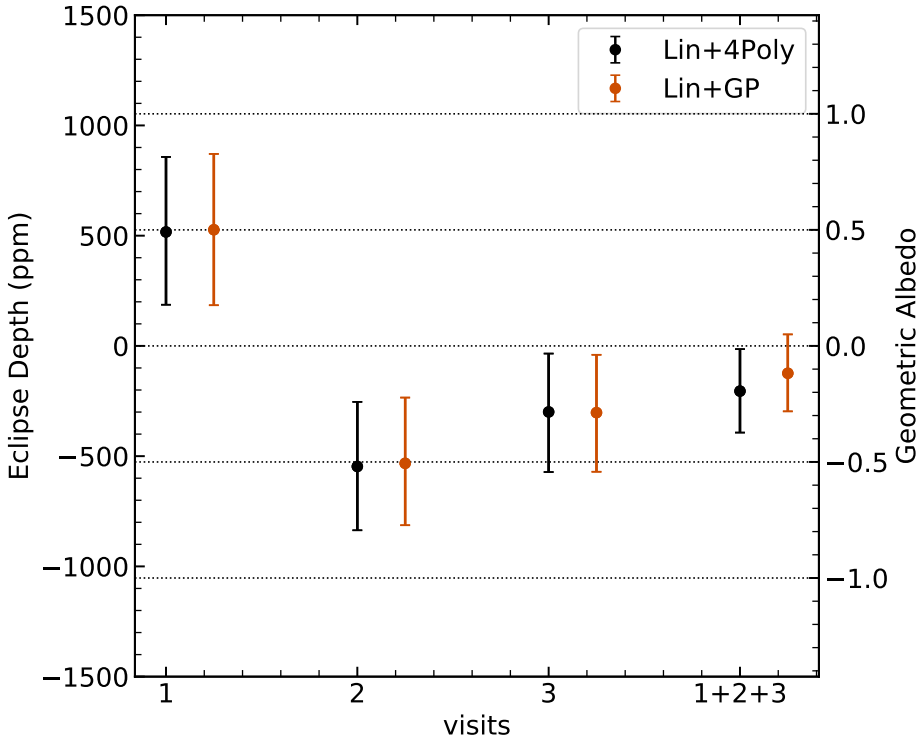

Fig. 2.3. A comparison of white light eclipse depths and the corresponding geometric albedo values. The points in black show the linear time ramp and 4th order polynomial fit, while the red points depict the linear time ramp and Gaussian Process fit. The x-axis marks all the three visits and 1+2+3 depicts the joint fit values. The error bars correspond to 1σ uncorrelated (white) noise values.

we divide the white light into wavebins of equal flux, instead of equal wavelength coverage. This choice keeps uncertainties to about the same magnitude in each wavebin.

We divided the white light into two, four and six wavebins of equal flux. We modeled each of these spectroscopic channels independently, with the priors being informed from the white light-curve fits. For each channel, we fit each visit individually, followed by a joint analysis across all the visits. The analysis methodology is similar to that of the white light-curve as described above in Section 2.3.

In Figure 2.4, we show a comparison of eclipse depths for each spectroscopic channel in our six wavebin analysis. Each panel is a wavelength bin, within which we plot best fit eclipse depth for each visit and the joint best fit eclipse depth. The points on the left (orange or green) are fourth order polynomial fits, plotted next to the GP fits (red or black). Again, the GP and fourth order polynomial methods give results consistent with each other.

Figure 2.5 shows a comparison of eclipse depth and the corresponding geometric albedo estimates for two (green), four(purple) and six(red) wavelength bins along with the white light eclipse depth (black) and the TESS best fit eclipse depth (blue).

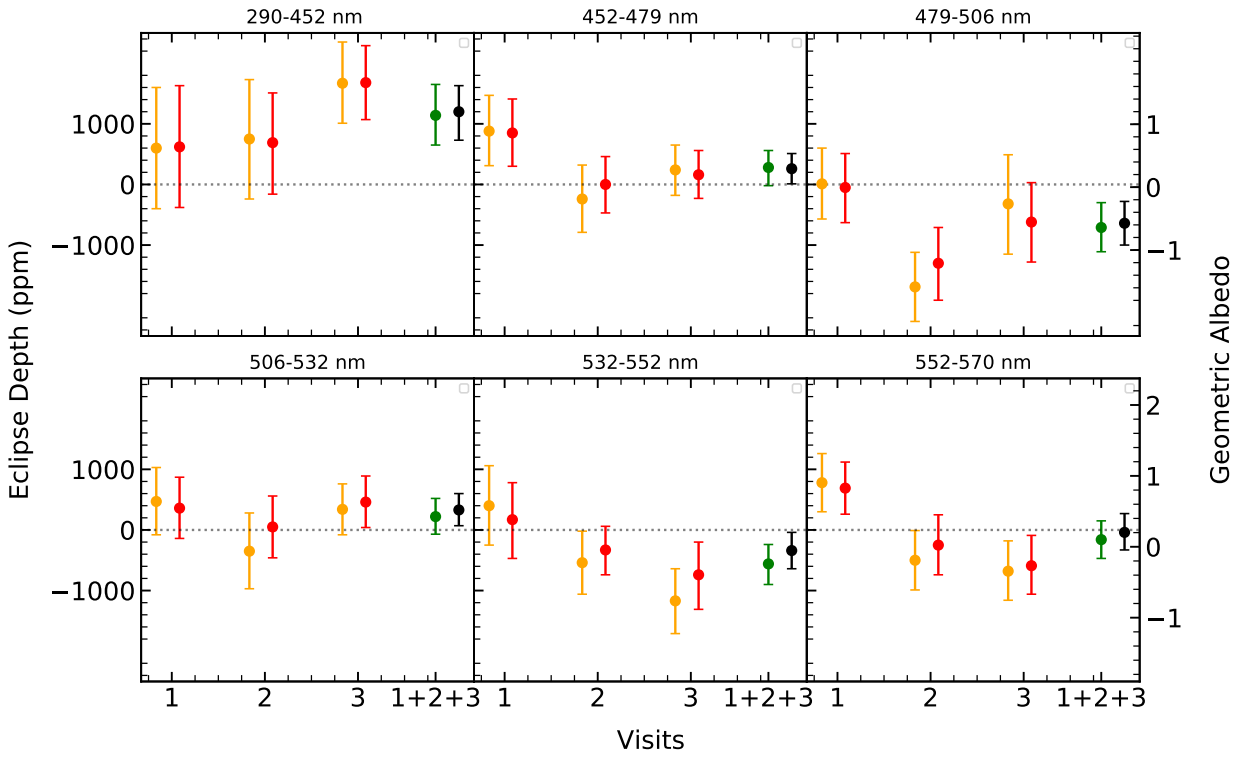

Fig. 2.4. A comparison of spectroscopic eclipse depths and the corresponding geometric albedo values. Each panel is a separate wavelength. For each one of these, all the three visits are compared, the polynomial fits (orange) versus the Gaussian process fit (red). The corresponding joint fits for each wavebin is also shown, with green points for polynomial fits and black points for Gaussian process fits. The error bars are 1 σ uncorrelated white noise.

2.3.4. TESS Light Curve Analysis

The TESS light-curve analysis is more straightforward than the HST analysis. It does not require consideration of correlated noise, because TESS obtains the data continuously unlike HST's orbits. Thus, TESS data could be detrended using the conventional methods. The 27 transits and 28 eclipses were detrended using a running median filter. The transits were fit jointly in order to determine the following orbital/system parameters: the period P, the mid-transit time T_c, the transit depth δ, the orbital semi-amplitude (in units of Rstar) aRs, the impact parameter b, the light-curve scatter and linear limb-darkening parameter $ld0$. These parameters were then fixed in order to fit the eclipses. As the eclipse depth is very small, the mid-eclipse time was fixed at the known phase of 0.5 (Gillon et al., 2012) in order to avoid fitting noise over the eclipses. The resulting eclipse depth is recorded in Table 2.1.

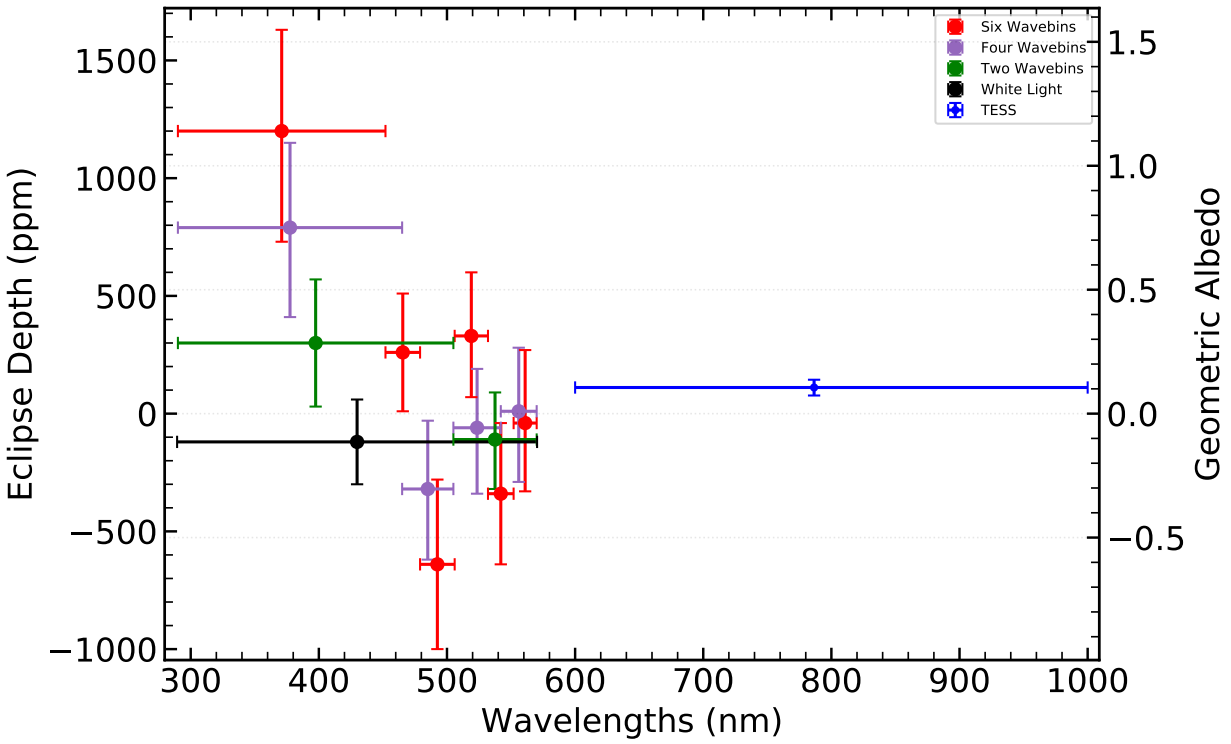

Fig. 2.5. A comparison of eclipse depths for 6, 4 and 2 wavelength bins and the white light eclipse depths. The second y-axis depicts the corresponding geometric albedo values. The red points show the 6 wavelength bins fits, the purple are for 4 bins, the green show 2 bins and the black is for white light fit. The TESS data point is shown in blue. All error bars show 1σ white noise uncertainty.

2.4. Results

2.4.1. Albedo Constraints

The best fit GP models for the three visits are shown in Figure 2.2 with the corrected lightcurves in the middle panels, and residuals in the bottom. The measured eclipse depths are reported in Table 2.1 for all wavelength channels. Table 2.1 also lists the inferred geometric albedo A_g measurements, calculated using equation 2.1.1 with the measured eclipse depth values, $R_p = 1.036 \pm 0.019\ R_j$, and $a = 0.01526 \pm 0.00018$ AU (Gillon et al., 2012). The corresponding errors propagate in quadrature.

In the white light joint analysis of all the three visits, we do not see any significant measurement of eclipse depth, i.e. all are consistent with zero eclipse depth. We give a 97.5% confidence upper limit on white light geometric albedo measurement across the STIS bandpass at 0.25. This means that WASP-43b reflects 25% of the light it receives in the 290-570 nm waveband at full phase. On the other hand, the TESS best fit constrains the white light geometric albedo measurement in the $600 - 1000$ nm waveband to 0.17, implying that only 17% of the light in this waveband is reflected at full phase. During the fitting,

we also allow for negative eclipse depths. Since any measurement of a real quantity has an associated error, the fitting routine should be able to take into account the possibility of a negative measurement. A negative eclipse depth, in reality, is unphysical, and so will the corresponding negative geometric albedo.

The most striking result is that the measured albedo in the wavelength range 290-505 is higher than that measured in the 505-570 nm range. This potential increase in the geometric albedo towards the shorter wavelengths, is also visible in our four and six wavebin analysis as shown in Figure 2.5. This is similar to the case of HD 189733b (Evans et al., 2013) and in stark contrast to WASP-12b (Bell et al., 2017).

2.4.2. Atmosphere and Clouds

The stellar irradiation is the greatest at optical wavelengths, thus, understanding both absorption and scattering phenomenon occurring at these wavelengths is crucial in determining the global energy budgets of hot Jupiters. For the case of hot Jupiters, the UV/optical reflection spectra is sculpted by Rayleigh scattering by molecules and condensates and also absorption from alkalis such as Na, K and perhaps even TiO/VO (Seager & Sasselov, 2000; Sudarsky et al., 2000). The strengths and widths of these absorption features is highly sensitive to the abundances. If clouds are present, they mask the broad absorption wings of the alkali lines, particularly Na at 589 nm. Lecavelier Des Etangs et al. (2008a) identified enstatite ($MgSiO_3$) is one of the most likely constituent for haze particles, being transparent in the visible and formed of atoms abundant in hot atmospheres, and would produce a high albedo if present in sufficient quantity.

Previous studies have shown that a diverse range of atmospheric models could explain the obtained eclipse depths for the case of HD 189733b (Evans et al., 2013; Barstow et al., 2014). A degeneracy exists between the sizes of particles in a highly reflective mineral cloud and the abundance of optical absorbers. Data was found to be consistent for both large 10 μm particles with low absorber abundances and ≤ 1 μm particles with much more abundant alkali species.

We can perform a similar study for WASP-43b in order to gain insight into the absorbers and scatterers within the atmosphere. We use the `NEMESIS` spectral retrieval tool (Irwin et al., 2008; Barstow et al., 2014) to produce the predicted model spectra. `NEMESIS` is not a radiative equilibrium code instead it takes an atmospheric model and calculates the incident and emergent flux, but does not take into account heating from incoming stellar radiation. Shown in Figure 2.6 are four scenarios which take into account optical absorber alkali species Na and the highly reflective mineral clouds consisting Enstatite ($MgSiO_3$): 1. The blue curve shows 1 μm enstatite particles with Solar (1×) Na abundance 2. the orange curve shows the same size particles with 10×Na abundance 3. The light green curve shows a cloudfree

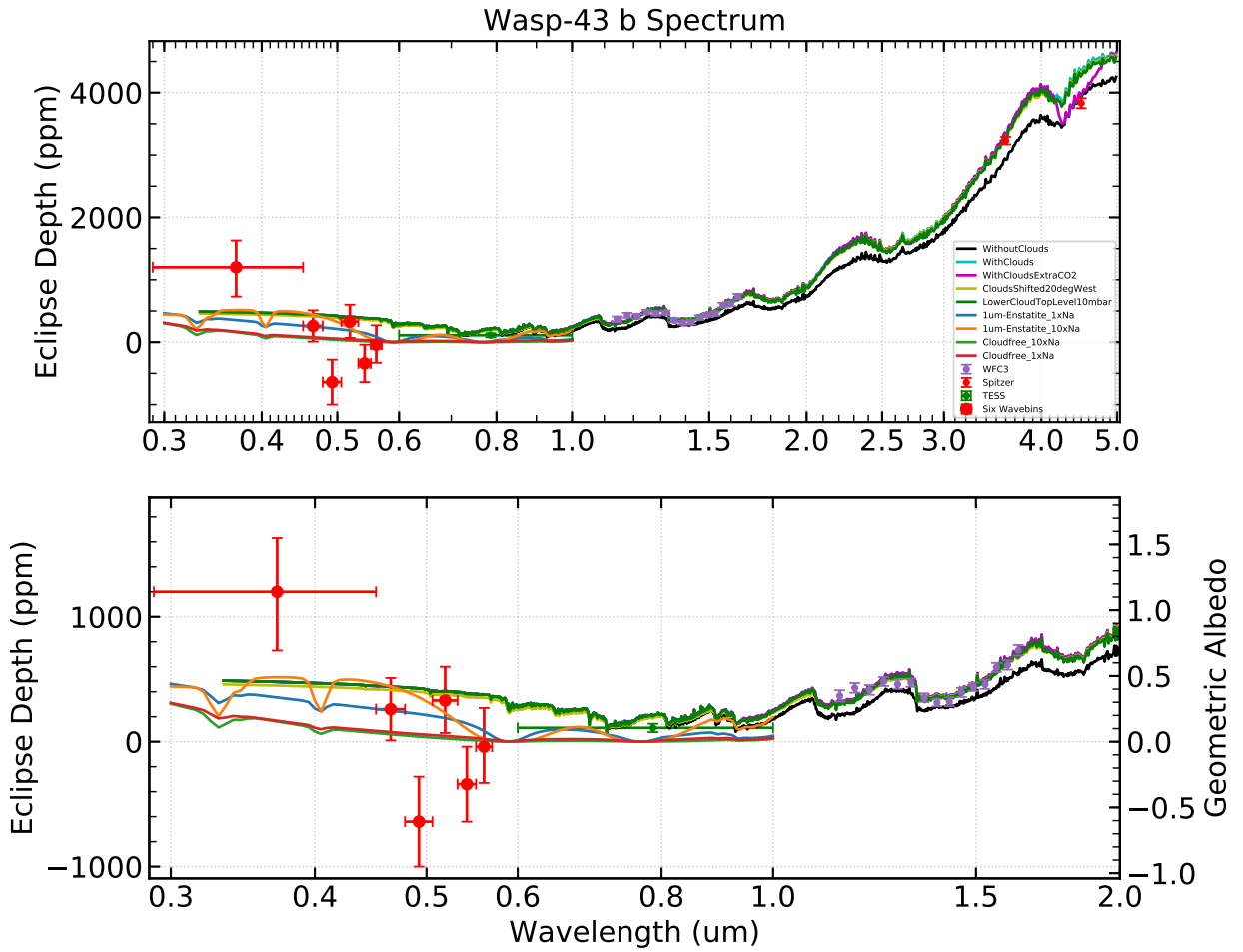

Fig. 2.6. *Top*: Joint best fit eclipse depths for WASP-43b (red) overplotted on predicted emission spectra from Mendonça et al. (2018). The different solid lines correspond to different atmospheric scenarios: black-cloudfree; cyan-with clouds; magenta-with clouds and extra CO_2; yellow-clouds in the nightside shifted 20^o westwards; green-clouds with lower cloud top level (20mbar instead of 10mbar). Simulated reflection spectra from our own NEMESIS simulations are also plotted - blue curve shows 1 μm enstatite particles with Solar (1×)Na abundance, while the orange curve shows the same particles with 10×Na; light green curve shows a cloudfree scenario with 10×Na while red curve shows cloudfree with 1×Na abundance. The purple points are WFC3/HST data from Stevenson et al. (2014b) and dark red points at $3.6\mu m$ and $4.5\mu m$ are Spitzer datapoints from Stevenson et al. (2017). *Bottom*: Zoom in on only the UV/optical/Near-IR wavelengths, with corresponding geometric albedo measurements on the secondary y-axis.

scenario with 10×Na abundance and 4. the red curve that shows the same cloudfree scenario with 1×Na abundance.

We also plot for comparison, previously published emission spectra predicted for WASP-43b from Mendonça et al. (2018). The authors develop THOR GCM from scratch, where instead of solving the primitive equations of meteorology that assume hydrostatic equilibrium, a thin atmosphere and neglect radial Coriolis terms, they use a different approach.

Table 2.2. Chi Square Values for our own simulations of reflected light models for six wavebins of HST/STIS and TESS data point

Model Name	Total χ^2
1μm Enstatite, 1×Na	15.9125
1μm Enstatite, 10×Na	13.8973
Cloudfree, 1×Na	22.4445
Cloudfree, 10×Na	20.5868

They include a simpler 'double-gray' radiative transfer where radiation is split into the optical/visible (from the star) and infrared (from the exoplanet) wavebands but solved the non-hydrostatic Euler equations. The outputs of these GCMs are then post-processed to produce emission spectra in the following five idealized scenarios: a cloud-free atmosphere shown by black curves; a cloudy atmosphere with a cloud deck on the nightside extending to a cloud-top pressure of 10 mbar shown by cyan curves; a cloudy atmosphere with nightside cloud deck and enhanced CO_2 shown by magenta curves; a cloudy atmosphere with cloud deck shifted westwards in longitude by 20^o shown by yellow curves that physically mimics the protrusion of the cloud deck from the nightside into the dayside caused by atmospheric circulation and the presence of mid-latitude cold vortices; and lastly, a cloudy atmosphere with cloud top at 20 mbar instead of 10 mbar shown with green curves, that mimics variation in the microphysical cloud processes and atmospheric mixing.

In the UV/optical regime, the models from Mendonça et al. (2018) are not significantly different with respect to the uncertainties on our HST/STIS data. Therefore, we are unable to distinguish amongst them. But our own simulations using the `NEMESIS` do show a considerable variation in this regime, and our data could help choose more probable scenarios amongst these.

According to the chi-square values listed in Table 2.2, the limits from our HST/STIS and TESS data points give a χ^2 per datum (χ^2/N_{obs}, $N_{obs} = 7$) of about 2.3 for 1 μm Enstatite particles and 1×Na, 2.0 for same size Enstatite particles and 10×Na, 3.2 for cloudfree with 10×Na and 2.9 for cloudfree and 1×Na scenario. Although, none of the scenarios considered here capture the data at hand completely and end up underestimating the error variance of the data, but a weakly favourable scenario could be the cloudy atmosphere with 1μm Enstatite particles and 10×Na. Further modelling of the optical regime of the spectrum is required to conclusively demonstrate the presence of clouds or haze along with alkali species abundances.

2.5. Discussion

With our measurements of the spectrally resolved geometric albedo for WASP-43b, we can fully constrain the amount of energy reflected. The hot Jupiter Albedo Problem described

an apparent discrepancy where the Bond albedos for hot Jupiters were measured to be greater than the geometric albedos. The most likely solution proposed here was to measure substantially higher geometric albedos beyond the Kepler bandpass (Schwartz & Cowan, 2015). Our measured geometric albedo in the 290-505 nm range has a 97.5% confidence upper limit of 0.8 and of 0.28 in the 505-570 nm range. Therefore, we conclude that the discrepancy in the measured albedo values does not exist for WASP-43b, as we are able to measure high geometric albedos at shorter wavelengths.

Our results are similar to the ones obtained by Evans et al. (2013) for HD 189733b and different from those reported by Bell et al. (2017) for WASP-12b. This similarity is expected and can be partially understood in terms of equilibrium temperatures. HD 189733b has a similar equilibrium temperature of about 1400K to WASP-43b, while WASP-12b is an ultra-hot Jupiter with an equilibrium temperature of about 2500K. Clouds are feasible at cooler temperatures, where molecules can condense, thus both WASP-43b and HD 189733b are expected to have clouds.

The measured eclipse depths have high uncertainties, especially at shorter wavelengths. This is due to lower stellar flux (Figure 2.1) and poor detector sensitivity. This limited precision hinders ruling out more intricate scenarios of atmosphere composition and structure, such as a combination of haze and cloud layers or absorbers other than Na.

Since our dataset is comprised of three visits, i.e. three independent measurements of the eclipse depth, we are also able to check for consistency. Evidently, as Figure 2.3 depicts, Visit 1 is systematically higher in geometric albedo than visits 2 and 3. The spectroscopic comparison in Figure 2.4 shows inconsistencies among visits at all wavelengths. Therefore, a joint analysis of multiple visits is important in obtaining a robust result. Since previous measurements of reflected light for HD 189733b and WASP-12b are only based on a single measurement, their derived results should not be taken at face value.

Our comparison of the fourth order polynomial and GP methods gave essentially similar results. However, the GP method does give eclipse depths that are more consistent with each other. Gaussian Processes, we maintain, is a more robust method of fitting the systematics, especially for more complicated scenarios, as has been showed amply in the literature. Since it does not confine to any specific analytical function, the eclipse depths obtained are more accurate and can be easily compared across the literature.

Our results, along with HD 189733b show that the hot Jupiters might be more reflecting towards the shorter wavelengths, and would have cloudy daysides. But, ultra-hot Jupiters like WASP-12b, do not seem to follow the trend. Our dataset is the third piece in the growing puzzle of optical albedo measurements for exoplanets, and sets the stage for new observations to come.

Above 600 nm, the upcoming James Webb Space Telescope will revolutionize the infrared picture of exoplanets. Nevertheless, below this cutoff, where reflection dominates thermal

emissions, this dataset will prove to be indispensable in the complete characterization of WASP-43b, and hot Jupiters in general.

Chapter 3

Conclusion and Next Steps

Hot Jupiters are the most amenable targets to atmospheric characterization. In this thesis, we chose to work with a well characterized hot Jupiter, WASP-43b. It has been observed in transit in the optical-nearIR-IR wavebands, but eclipse observations have been limited to the IR. Optical observations of hot Jupiters are as crucial as other wavebands, since they contain unique information about the reflectivity of the atmosphere. If we can constrain reflection properties, we can also define the energy budget of the planet by putting constraints on the amount of energy available to circulate around the planet. The energy budget will then feed back into the composition, temperature structure and physical properties like the presence of clouds or haze particles.

Measuring the reflection spectra was also required to solve the empirical discrepancy called the hot Jupiter Albedo Problem. One would imagine that it would be easy to determine the amount of light reflected, once we knew the amount of light emitted by the planet via energy conservation calculations. Astronomers then tried to measure the Bond Albedo in the IR, but subsequent measurements of reflected light via Kepler, CoRoT and MOST found very low geometric albedo values that did not completely account for all the light. The most likely solution could be that the hot Jupiters would have substantially higher geometric albedos beyond the Kepler band pass, and therefore need more detections below ~ 420 nm.

At these wavelengths, only space based observations can provide accurate enough resolution to measure the reflected light, since the eclipse method requires at least an order of magnitude higher photometric precision than transit observations of the same planet because the planet will be fainter than its host star, while the occulted area remains the same. Also, since the star emits most of its light at optical wavelengths, the planet could be easily washed away. Today, only the Space Telescope Imaging Spectrograph (STIS) onboard

the Hubble Space Telescope (HST) is capable of procuring UV-optical eclipse observations.

So, we used the HST/STIS instrument and observed the WASP-43b eclipse three times. We reduced the obtained data to white light-curves and fit the eclipse depth by allowing Gaussian Processes to handle the orbit-long systematics in conjunction with a linear time ramp that modeled the visit-long slope.

Previous similar measurements of HD 189733b and WASP-12b only took one observation, but having three allowed consistency checks. And clearly, as shown in the thesis, the first observation in white light was systematically different than the other two. It is not always possible to know why a given measurement was different than the rest, and multiple observations help mitigate the effects of such systematics. We obtain an upper limit at 97.5% confidence of 0.25 signifying low geometric albedo in the white light HST/STIS 290-570 nm waveband.

We also binned the data into 2, 4 and 6 wavelength bins of equal flux instead of equal wavelength coverage, and performed a separate analysis for each set. We set upper limits of 0.8 and 0.28 for the shorter and longer HST/STIS wavelength bins, in the 2 wavebin analysis, respectively. These measurements show that the spectroscopic geometric albedo showed a potential increase towards the shorter wavelengths, just like HD 189733b. This could be a positive move towards solving the Albedo Problem for WASP-43b.

We also compare our systematics' fits to the traditional method of using a fourth order polynomial and find nearly consistent results. Gaussian Processes, however, is a more robust method of fitting the systematics, especially for more complicated scenarios, as has been showed amply in the literature. The exoplanet community is already awakening towards its power, and we propose to use Gaussian Processes for future exoplanet studies.

Along with the HST data that our team obtained, we took 600-1000 nm eclipse observation data from the recently launched TESS mission. We fit the white light-curves and put an 97.5% confidence upper limit of 0.17 on the geometric albedo.

In order to infer atmospheric properties, we employed the NEMESIS tool to model various scenarios including both cloudy and cloudfree kinds with different particle sizes. We find that WASP-43b favours a cloudy atmosphere with enstatite particles of size 1μm and 10$\times$ Solar Na abundance. However, the modest precision of the dataset especially at shorter wavelengths does not allow in depth atmospheric characterization of the atmosphere

of WASP-43b.

When compared with the literature, WASP-43b is similar to the previously published blue exoplanet HD 189733b. With a similar equilibrium temperature, both hot Jupiters exhibited similar optical geometric albedo properties. Both show an increase in the geometric albedo towards shorter wavelengths. However, this trend may not be generalized for exoplanets, since the ultra-hot Jupiter WASP-12b was measured to be 'dark', i.e. non-reflecting. The fact that the first three exoplanets with optical albedo spectra exhibit differences points to the importance of spectrally resolved reflected light observations.

As next steps, before the article is submitted for publication, the dataset can be further analysed. We assumed, in general, that the reflected light dominates at shorter wavelengths. But as we move towards higher wavelengths, the flux measured has a larger thermal component especially near 1 micron. Therefore, especially for the TESS data point, that lies in the 600-1000 nm wavelength range, we still need to check the actual component of reflected light versus thermal light. An atmospheric retrieval in these wavelengths that would include all the previous transit and eclipse measurements could help inform us about the contribution of reflected light. Once we understand that, we could claim the composition of the atmosphere.

References

Agol, E., Cowan, N. B., Knutson, H. A., et al. 2010, apj, 721, 1861, doi: 10.1088/0004-637X/721/2/1861

Agúndez, M., Parmentier, V., Venot, O., Hersant, F., & Selsis, F. 2014, aap, 564, A73, doi: 10.1051/0004-6361/201322895

Alonso, R., Brown, T. M., Torres, G., et al. 2004, apjl, 613, L153, doi: 10.1086/425256

Anders, E., & Grevesse, N. 1989, gca, 53, 197, doi: 10.1016/0016-7037(89)90286-X

Arcangeli, J., Désert, J.-M., Line, M. R., et al. 2018, apj, 855, L30, doi: 10.3847/2041-8213/aab272

Barge, P., Baglin, A., Auvergne, M., et al. 2008, aap, 482, L17, doi: 10.1051/0004-6361:200809353

Barstow, J. K., Aigrain, S., Irwin, P. G. J., et al. 2014, apj, 786, 154, doi: 10.1088/0004-637X/786/2/154

Bell, T. J., Nikolov, N., Cowan, N. B., et al. 2017, The Astrophysical Journal, 847, L2, doi: 10.3847/2041-8213/aa876c

Benneke, B., & Seager, S. 2012, apj, 753, 100, doi: 10.1088/0004-637X/753/2/100

Benneke, B., Werner, M., Petigura, E., et al. 2017, apj, 834, 187, doi: 10.3847/1538-4357/834/2/187

Benneke, B., Knutson, H. A., Lothringer, J., et al. 2019, Nature Astronomy, 3, 813, doi: 10.1038/s41550-019-0800-5

Berta, Z. K., Charbonneau, D., Désert, J.-M., et al. 2012, apj, 747, 35, doi: 10.1088/0004-637X/747/1/35

Birkby, J. L., de Kok, R. J., Brogi, M., et al. 2013, mnras, 436, L35, doi: 10.1093/mnrasl/slt107

Blecic, J., Harrington, J., Madhusudhan, N., et al. 2014, The Astrophysical Journal, 781, 116, doi: 10.1088/0004-637X/781/2/116

Brogi, M., de Kok, R. J., Birkby, J. L., Schwarz, H., & Snellen, I. A. G. 2014, aap, 565, A124, doi: 10.1051/0004-6361/201423537

Brown, T. M., Charbonneau, D., Gilliland, R. L., Noyes, R. W., & Burrows, A. 2001, The Astrophysical Journal, 552, 699, doi: 10.1086/320580

Burkert, A., Lin, D. N. C., Bodenheimer, P. H., Jones, C. A., & Yorke, H. W. 2005, apj, 618, 512, doi: 10.1086/425955

Burrows, A., & Sharp, C. M. 1999, apj, 512, 843, doi: 10.1086/306811

Campbell, B., Walker, G. A. H., & Yang, S. 1988, apj, 331, 902, doi: 10.1086/166608

Chapman, J. W., Zellem, R. T., Line, M. R., et al. 2017, Publications of the Astronomical Society of the Pacific, 129, 104402, doi: 10.1088/1538-3873/aa84a9

Charbonneau, D., Brown, T. M., Noyes, R. W., & Gilliland, R. L. 2002, apj, 568, 377, doi: 10.1086/338770

Charbonneau, D., Noyes, R. W., Korzennik, S. G., et al. 1999, apjl, 522, L145, doi: 10.1086/312234

Charbonneau, D., Allen, L. E., Megeath, S. T., et al. 2005, apj, 626, 523, doi: 10.1086/429991

Chen, G., van Boekel, R., Wang, H., et al. 2014, Astronomy and Astrophysics, 563, A40, doi: 10.1051/0004-6361/201322740

Cho, J. Y.-K., Menou, K., Hansen, B. M. S., & Seager, S. 2003, apjl, 587, L117, doi: 10.1086/375016

Cooper, C. S., & Showman, A. P. 2006, apj, 649, 1048, doi: 10.1086/506312

Cowan, N. B., & Agol, E. 2008, apj, 678, L129, doi: 10.1086/588553

—. 2011a, apj, 729, 54, doi: 10.1088/0004-637X/729/1/54

—. 2011b, apj, 726, 82, doi: 10.1088/0004-637X/726/2/82

Crossfield, I. J. M. 2015, Publications of the Astronomical Society of the Pacific, 127, 941, doi: 10.1086/683115

Crossfield, I. J. M., Barman, T., Hansen, B. M. S., & Howard, A. W. 2013, aap, 559, A33, doi: 10.1051/0004-6361/201322278

Cushing, M. C., Roellig, T. L., Marley, M. S., et al. 2006, apj, 648, 614, doi: 10.1086/505637

Dai, F., Winn, J. N., Yu, L., & Albrecht, S. 2017, The Astronomical Journal, 153, 40, doi: 10.3847/1538-3881/153/1/40

de Kok, R. J., Brogi, M., Snellen, I. A. G., et al. 2013, aap, 554, A82, doi: 10.1051/0004-6361/201321381

Deming, D., Seager, S., Richardson, L. J., & Harrington, J. 2005, nat, 434, 740, doi: 10.1038/nature03507

Deming, D., Wilkins, A., McCullough, P., et al. 2013, apj, 774, 95, doi: 10.1088/0004-637X/774/2/95

Demory, B.-O., de Wit, J., Lewis, N., et al. 2013, apj, 776, L25, doi: 10.1088/2041-8205/776/2/L25

Demory, B.-O., Ehrenreich, D., Queloz, D., et al. 2015, Monthly Notices of the Royal Astronomical Society, 450, 2043, doi: 10.1093/mnras/stv673

Demory, B.-O., Gillon, M., de Wit, J., et al. 2016, nat, 532, 207, doi: 10.1038/nature17169

Désert, J.-M., Lecavelier des Etangs, A., Hébrard, G., et al. 2009, apj, 699, 478, doi: 10.1088/0004-637X/699/1/478

Diamond-Lowe, H., Stevenson, K. B., Bean, J. L., Line, M. R., & Fortney, J. J. 2014, apj, 796, 66, doi: 10.1088/0004-637X/796/1/66

Dobbs-Dixon, I., Agol, E., & Deming, D. 2015, apj, 815, 60, doi: 10.1088/0004-637X/815/1/60

Dragomir, D., Benneke, B., Pearson, K. A., et al. 2015, apj, 814, 102, doi: 10.1088/0004-637X/814/2/102

Dyudina, U. A., Sackett, P. D., Bayliss, D. D. R., et al. 2005, apj, 618, 973, doi: 10.1086/426050

Ehrenreich, D., Bourrier, V., Wheatley, P. J., et al. 2015, nat, 522, 459, doi: 10.1038/nature14501

Evans, T. M., Pont, F., Sing, D. K., et al. 2013, The Astrophysical Journal, 772, L16, doi: 10.1088/2041-8205/772/2/L16

Evans, T. M., Sing, D. K., Wakeford, H. R., et al. 2016, apjl, 822, L4, doi: 10.3847/2041-8205/822/1/L4

Evans, T. M., Sing, D. K., Kataria, T., et al. 2017, nat, 548, 58, doi: 10.1038/nature23266

Foreman-Mackey, D., Hogg, D. W., Lang, D., & Goodman, J. 2013, Publications of the Astronomical Society of the Pacific, 125, 306, doi: 10.1086/670067

Fortney, J. J. 2005, mnras, 364, 649, doi: 10.1111/j.1365-2966.2005.09587.x

Fortney, J. J., Lodders, K., Marley, M. S., & Freedman, R. S. 2008, apj, 678, 1419, doi: 10.1086/528370

Fortney, J. J., Mordasini, C., Nettelmann, N., et al. 2013, apj, 775, 80, doi: 10.1088/0004-637X/775/1/80

Garcia Munoz, A., & Isaak, K. G. 2015, Proceedings of the National Academy of Science, 112, 13461, doi: 10.1073/pnas.1509135112

Gaudi, B. S., Seager, S., & Mallen-Ornelas, G. 2005, apj, 623, 472, doi: 10.1086/428478

Gibson, N. P., Aigrain, S., Barstow, J. K., et al. 2013, Monthly Notices of the Royal Astronomical Society, 428, 3680, doi: 10.1093/mnras/sts307

Gibson, N. P., Aigrain, S., Roberts, S., et al. 2012a, Monthly Notices of the Royal Astronomical Society, 419, 2683, doi: 10.1111/j.1365-2966.2011.19915.x

Gibson, N. P., Pont, F., & Aigrain, S. 2011, Monthly Notices of the Royal Astronomical Society, 411, 2199, doi: 10.1111/j.1365-2966.2010.17837.x

Gibson, N. P., Aigrain, S., Pont, F., et al. 2012b, Monthly Notices of the Royal Astronomical Society, 422, 753, doi: 10.1111/j.1365-2966.2012.20655.x

Gillon, M., Triaud, A. H. M. J., Fortney, J. J., et al. 2012, Astronomy and Astrophysics, 542, A4, doi: 10.1051/0004-6361/201218817

Griffith, C. A., Turner, J. D., Zellem, R., Tinetti, G., & Teske, J. 2013, in European Planetary Science Congress, EPSC2013–883

Guillot, T., Burrows, A., Hubbard, W. B., Lunine, J. I., & Saumon, D. 1996, apjl, 459, L35, doi: 10.1086/309935

Hatzes, A. P., & Cochran, W. D. 1993, apj, 413, 339, doi: 10.1086/173002

Haynes, K., Mandell, A. M., Madhusudhan, N., Deming, D., & Knutson, H. 2015, apj, 806, 146, doi: 10.1088/0004-637X/806/2/146

Hellier, C., Anderson, D. R., Collier Cameron, A., et al. 2011, Astronomy and Astrophysics, 535, L7, doi: 10.1051/0004-6361/201117081

Heng, K. 2016, apj, 826, L16, doi: 10.3847/2041-8205/826/1/L16

Heng, K., & Demory, B.-O. 2013, apj, 777, 100, doi: 10.1088/0004-637X/777/2/100

Hu, R., Demory, B.-O., Seager, S., Lewis, N., & Showman, A. P. 2015, apj, 802, 51, doi: 10.1088/0004-637X/802/1/51

Hubeny, I., Burrows, A., & Sudarsky, D. 2003, apj, 594, 1011, doi: 10.1086/377080

Huitson, C. M., Sing, D. K., Vidal-Madjar, A., et al. 2012, mnras, 422, 2477, doi: 10.1111/j.1365-2966.2012.20805.x

Huitson, C. M., Sing, D. K., Pont, F., et al. 2013, mnras, 434, 3252, doi: 10.1093/mnras/stt1243

Iro, N., Bézard, B., & Guillot, T. 2005, aap, 436, 719, doi: 10.1051/0004-6361:20048344

Irwin, P. G. J., Teanby, N. A., de Kok, R., et al. 2008, jqsrt, 109, 1136, doi: 10.1016/j.jqsrt.2007.11.006

Jenkins, J. M., Tenenbaum, P., Seader, S., et al. 2017, Kepler Data Processing Handbook: Transiting Planet Search, Tech. rep.

Jenkins, J. M., Caldwell, D. A., Chandrasekaran, H., et al. 2010, apjl, 713, L87, doi: 10.1088/2041-8205/713/2/L87

Jenkins, J. M., Twicken, J. D., McCauliff, S., et al. 2016, Society of Photo-Optical Instrumentation Engineers (SPIE) Conference Series, Vol. 9913, The TESS science processing operations center, 99133E, doi: 10.1117/12.2233418

Kammer, J. A., Knutson, H. A., Line, M. R., et al. 2015, apj, 810, 118, doi: 10.1088/0004-637X/810/2/118

Kataria, T., Showman, A. P., Fortney, J. J., et al. 2015, apj, 801, 86, doi: 10.1088/0004-637X/801/2/86

Kataria, T., Sing, D. K., Lewis, N. K., et al. 2016, apj, 821, 9, doi: 10.3847/0004-637X/821/1/9

Keating, D., & Cowan, N. B. 2017, apjl, 849, L5, doi: 10.3847/2041-8213/aa8b6b

Kipping, D. M., & Spiegel, D. S. 2011, Monthly Notices of the Royal Astronomical Society, 417, L88, doi: 10.1111/j.1745-3933.2011.01127.x

Knutson, H. A., Benneke, B., Deming, D., & Homeier, D. 2014, nat, 505, 66, doi: 10.1038/nature12887

Knutson, H. A., Charbonneau, D., Allen, L. E., Burrows, A., & Megeath, S. T. 2008, apj, 673, 526, doi: 10.1086/523894

Knutson, H. A., Charbonneau, D., Noyes, R. W., Brown, T. M., & Gilliland, R. L. 2007a, apj, 655, 564, doi: 10.1086/510111

Knutson, H. A., Charbonneau, D., Allen, L. E., et al. 2007b, nat, 447, 183, doi: 10.1038/nature05782

Knutson, H. A., Charbonneau, D., Cowan, N. B., et al. 2009, apj, 690, 822, doi: 10.1088/0004-637X/690/1/822

Knutson, H. A., Lewis, N., Fortney, J. J., et al. 2012, apj, 754, 22, doi: 10.1088/0004-637X/754/1/22

Komacek, T. D., & Showman, A. P. 2016, apj, 821, 16, doi: 10.3847/0004-637X/821/1/16

Komacek, T. D., Showman, A. P., & Tan, X. 2017, apj, 835, 198, doi: 10.3847/1538-4357/835/2/198

Konacki, M., Torres, G., Jha, S., & Sasselov, D. D. 2003, nat, 421, 507, doi: 10.1038/nature01379

Kreidberg, L. 2015, Publications of the Astronomical Society of the Pacific, 127, 1161, doi: 10.1086/683602

—. 2018, Exoplanet Atmosphere Measurements from Transmission Spectroscopy and Other Planet Star Combined Light Observations, 100, doi: 10.1007/978-3-319-55333-7_100

Kreidberg, L., Bean, J. L., Désert, J.-M., et al. 2014a, apjl, 793, L27, doi: 10.1088/2041-8205/793/2/L27

—. 2014b, nat, 505, 69, doi: 10.1038/nature12888

Kreidberg, L., Line, M. R., Bean, J. L., et al. 2015, apj, 814, 66, doi: 10.1088/0004-637X/814/1/66

Kreidberg, L., Line, M. R., Parmentier, V., et al. 2018, aj, 156, 17, doi: 10.3847/1538-3881/aac3df

Latham, D. W., Mazeh, T., Stefanik, R. P., Mayor, M., & Burki, G. 1989, nat, 339, 38, doi: 10.1038/339038a0

Lecavelier Des Etangs, A., Pont, F., Vidal-Madjar, A., & Sing, D. 2008a, aap, 481, L83, doi: 10.1051/0004-6361:200809388

Lecavelier Des Etangs, A., Vidal-Madjar, A., Désert, J. M., & Sing, D. 2008b, aap, 485, 865, doi: 10.1051/0004-6361:200809704

Lee, G., Dobbs-Dixon, I., Helling, C., Bognar, K., & Woitke, P. 2016, aap, 594, A48, doi: 10.1051/0004-6361/201628606

Line, M. R., & Parmentier, V. 2016, apj, 820, 78, doi: 10.3847/0004-637X/820/1/78

Line, M. R., Stevenson, K. B., Bean, J., et al. 2016, aj, 152, 203, doi: 10.3847/0004-6256/152/6/203

Lothringer, J. D., Benneke, B., Crossfield, I. J. M., et al. 2018, aj, 155, 66, doi: 10.3847/1538-3881/aaa008

Madhusudhan, N., Harrington, J., Stevenson, K. B., et al. 2011, nat, 469, 64, doi: 10.1038/nature09602

Mandel, K., & Agol, E. 2002, apj, 580, L171, doi: 10.1086/345520

Mayor, M., & Queloz, D. 1995, nat, 378, 355, doi: 10.1038/378355a0

Mendonça, J. M., Malik, M., Demory, B.-O., & Heng, K. 2018, aj, 155, 150, doi: 10.3847/1538-3881/aaaebc

Miller-Ricci Kempton, E., Zahnle, K., & Fortney, J. J. 2012, apj, 745, 3, doi: 10.1088/0004-637X/745/1/3

Mordasini, C., van Boekel, R., Mollière, P., Henning, T., & Benneke, B. 2016, apj, 832, 41, doi: 10.3847/0004-637X/832/1/41

Morley, C. V., Fortney, J. J., Kempton, E. M. R., et al. 2013, apj, 775, 33, doi: 10.1088/0004-637X/775/1/33

Morley, C. V., Fortney, J. J., Marley, M. S., et al. 2015, apj, 815, 110, doi: 10.1088/0004-637X/815/2/110

Morley, C. V., Knutson, H., Line, M., et al. 2017, aj, 153, 86, doi: 10.3847/1538-3881/153/2/86

Moses, J. I., Madhusudhan, N., Visscher, C., & Freedman, R. S. 2013, apj, 763, 25, doi: 10.1088/0004-637X/763/1/25

Mousis, O., Fletcher, L. N., Lebreton, J. P., et al. 2014, Planetary and Space Science, 104, 29, doi: 10.1016/j.pss.2014.09.014

Murgas, F., Pallé, E., Zapatero Osorio, M. R., et al. 2014, Astronomy and Astrophysics, 563, A41, doi: 10.1051/0004-6361/201322374

Nikolov, N., Sing, D. K., Pont, F., et al. 2014, mnras, 437, 46, doi: 10.1093/mnras/stt1859

Nugroho, S. K., Kawahara, H., Masuda, K., et al. 2017, aj, 154, 221, doi: 10.3847/1538-3881/aa9433

Oreshenko, M., Heng, K., & Demory, B.-O. 2016, mnras, 457, 3420, doi: 10.1093/mnras/stw133

Parmentier, V., Fortney, J. J., Showman, A. P., Morley, C., & Marley, M. S. 2016, apj, 828, 22, doi: 10.3847/0004-637X/828/1/22

Parmentier, V., Showman, A. P., & de Wit, J. 2015, Experimental Astronomy, 40, 481, doi: 10.1007/s10686-014-9395-0

Parmentier, V., Showman, A. P., & Lian, Y. 2013, aap, 558, A91, doi: 10.1051/0004-6361/201321132

Pass, E. K., Cowan, N. B., Cubillos, P. E., & Sklar, J. G. 2019, mnras, 489, 941, doi: 10.1093/mnras/stz2226

Perez-Becker, D., & Showman, A. P. 2013, apj, 776, 134, doi: 10.1088/0004-637X/776/2/134

Pont, F., Knutson, H., Gilliland, R. L., Moutou, C., & Charbonneau, D. 2008, mnras, 385, 109, doi: 10.1111/j.1365-2966.2008.12852.x

Prinn, R. G., & Barshay, S. S. 1977, Science, 198, 1031, doi: 10.1126/science.198.4321.1031

Ricci, D., Ramón-Fox, F. G., Ayala-Loera, C., et al. 2015, Publications of the Astronomical Society of the Pacific, 127, 143, doi: 10.1086/680233

Robinson, T. D. 2017, apj, 836, 236, doi: 10.3847/1538-4357/aa5ea8

Robinson, T. D., Maltagliati, L., Marley, M. S., & Fortney, J. J. 2014, Proceedings of the National Academy of Science, 111, 9042, doi: 10.1073/pnas.1403473111

Rogers, J., López-Morales, M., Apai, D., & Adams, E. 2013, apj, 767, 64, doi: 10.1088/0004-637X/767/1/64

Rogers, T. M. 2017, Nature Astronomy, 1, 0131, doi: 10.1038/s41550-017-0131

Rowe, J. F., Matthews, J. M., Seager, S., et al. 2008, The Astrophysical Journal, 689, 1345, doi: 10.1086/591835

Schwartz, J. C., & Cowan, N. B. 2015, mnras, 449, 4192, doi: 10.1093/mnras/stv470

Schwartz, J. C., Kashner, Z., Jovmir, D., & Cowan, N. B. 2017, apj, 850, 154, doi: 10.3847/1538-4357/aa9567

Schwarz, H., Brogi, M., de Kok, R., Birkby, J., & Snellen, I. 2015, aap, 576, A111, doi: 10.1051/0004-6361/201425170

Seager, S. 2010, Exoplanet Atmospheres: Physical Processes

Seager, S., & Sasselov, D. D. 2000, apj, 537, 916, doi: 10.1086/309088

Sedaghati, E., Boffin, H. M. J., MacDonald, R. J., et al. 2017, nat, 549, 238, doi: 10.1038/nature23651

Showman, A. P., Cooper, C. S., Fortney, J. J., & Marley, M. S. 2008, apj, 682, 559, doi: 10.1086/589325

Showman, A. P., Fortney, J. J., Lian, Y., et al. 2009, apj, 699, 564, doi: 10.1088/0004-637X/699/1/564

Showman, A. P., & Guillot, T. 2002, aap, 385, 166, doi: 10.1051/0004-6361:20020101

Showman, A. P., & Ingersoll, A. P. 1998, icarus, 132, 205, doi: 10.1006/icar.1998.5898

Showman, A. P., & Polvani, L. M. 2011, apj, 738, 71, doi: 10.1088/0004-637X/738/1/71

Shporer, A., & Hu, R. 2015, aj, 150, 112, doi: 10.1088/0004-6256/150/4/112

Shporer, A., Wong, I., Huang, C. X., et al. 2019, aj, 157, 178, doi: 10.3847/1538-3881/ab0f96

Sing, D. K., Vidal-Madjar, A., Désert, J. M., Lecavelier des Etangs, A., & Ballester, G. 2008a, The Astrophysical Journal, 686, 658, doi: 10.1086/590075

Sing, D. K., Vidal-Madjar, A., Lecavelier des Etangs, A., et al. 2008b, apj, 686, 667, doi: 10.1086/590076

Sing, D. K., Désert, J.-M., Fortney, J. J., et al. 2011a, aap, 527, A73, doi: 10.1051/0004-6361/201015579

Sing, D. K., Pont, F., Aigrain, S., et al. 2011b, mnras, 416, 1443, doi: 10.1111/j.1365-2966.2011.19142.x

Sing, D. K., Lecavelier des Etangs, A., Fortney, J. J., et al. 2013, mnras, 436, 2956, doi: 10.1093/mnras/stt1782

Sing, D. K., Fortney, J. J., Nikolov, N., et al. 2016, Nature, 529, 59, doi: 10.1038/nature16068

Smith, J. C., Stumpe, M. C., Van Cleve, J. E., et al. 2012, pasp, 124, 1000, doi: 10.1086/667697

Snellen, I. A. G., Albrecht, S., de Mooij, E. J. W., & Le Poole, R. S. 2008, aap, 487, 357, doi: 10.1051/0004-6361:200809762

Stassun, K. G., Oelkers, R. J., Pepper, J., et al. 2018, aj, 156, 102, doi: 10.3847/1538-3881/aad050

Steinrueck, M. E., Parmentier, V., Showman, A. P., Lothringer, J. D., & Lupu, R. E. 2018, arXiv e-prints, arXiv:1808.02011. https://arxiv.org/abs/1808.02011

Stevenson, K. B. 2016, apj, 817, L16, doi: 10.3847/2041-8205/817/2/L16

Stevenson, K. B., Bean, J. L., Madhusudhan, N., & Harrington, J. 2014a, apj, 791, 36, doi: 10.1088/0004-637X/791/1/36

Stevenson, K. B., Harrington, J., Nymeyer, S., et al. 2010, nat, 464, 1161, doi: 10.1038/nature09013

Stevenson, K. B., Désert, J.-M., Line, M. R., et al. 2014b, Science, 346, 838, doi: 10.1126/science.1256758

Stevenson, K. B., Line, M. R., Bean, J. L., et al. 2017, aj, 153, 68, doi: 10.3847/1538-3881/153/2/68

Stumpe, M. C., Smith, J. C., Catanzarite, J. H., et al. 2014, pasp, 126, 100, doi: 10.1086/674989

Sudarsky, D., Burrows, A., & Pinto, P. 2000, apj, 538, 885, doi: 10.1086/309160

Tsai, S.-M., Dobbs-Dixon, I., & Gu, P.-G. 2014, apj, 793, 141, doi: 10.1088/0004-637X/793/2/141

Turco, R. P., Hamill, P., Toon, O. B., Whitten, R. C., & Kiang, C. S. 1979, Journal of Atmospheric Sciences, 36, 699, doi: 10.1175/1520-0469(1979)036<0699:AODMDA>2.0.CO;2

Vidal-Madjar, A., Lecavelier des Etangs, A., Désert, J.-M., et al. 2003, nat, 422, 143, doi: 10.1038/nature01448

Vidal-Madjar, A., Désert, J. M., Lecavelier des Etangs, A., et al. 2004, apj, 604, L69, doi: 10.1086/383347

Visscher, C., & Moses, J. I. 2011, apj, 738, 72, doi: 10.1088/0004-637X/738/1/72

Wakeford, H. R., & Sing, D. K. 2015, aap, 573, A122, doi: 10.1051/0004-6361/201424207

Wakeford, H. R., Visscher, C., Lewis, N. K., et al. 2017a, mnras, 464, 4247, doi: 10.1093/mnras/stw2639

Wakeford, H. R., Sing, D. K., Kataria, T., et al. 2017b, Science, 356, 628, doi: 10.1126/science.aah4668

Wang, W., van Boekel, R., Madhusudhan, N., et al. 2013, The Astrophysical Journal, 770, 70, doi: 10.1088/0004-637X/770/1/70

Webber, M. W., Lewis, N. K., Marley, M., et al. 2015, apj, 804, 94, doi: 10.1088/0004-637X/804/2/94

Williams, P. K. G., Charbonneau, D., Cooper, C. S., Showman, A. P., & Fortney, J. J. 2006, apj, 649, 1020, doi: 10.1086/506468

Winn, J. N. 2010, arXiv e-prints, arXiv:1001.2010. https://arxiv.org/abs/1001.2010

Wolszczan, A., & Frail, D. A. 1992, nat, 355, 145, doi: 10.1038/355145a0

Wong, I., Shporer, A., Becker, J. C., et al. 2019, arXiv e-prints, arXiv:1910.08524. https://arxiv.org/abs/1910.08524

Zhang, X., & Showman, A. P. 2017, apj, 836, 73, doi: 10.3847/1538-4357/836/1/73